

HST Photometry for the Halo Stars in the Leo Elliptical NGC 3377¹

William E. Harris

Department of Physics & Astronomy, McMaster University, Hamilton L8S 4M1, Canada

`harris@physics.mcmaster.ca`

Gretchen L. H. Harris

Department of Physics & Astronomy, University of Waterloo, Waterloo N2L 3G1, Canada

`glharris@astro.uwaterloo.ca`

Andrew C. Layden

Department of Physics and Astronomy, Bowling Green State University, 104 Overman Hall, Bowling Green, OH 43403

`layden@baade.bgsu.edu`

Peter B. Stetson

Dominion Astrophysical Observatory, Herzberg Institute of Astrophysics, National Research Council, 5071 West Saanich Road, Victoria, V9E 2E7, Canada

`peter.stetson@nrc-cnrc.gc.ca`

ABSTRACT

We have used the ACS camera on HST to obtain (V, I) photometry for 57,000 red-giant stars in the halo of the Leo elliptical NGC 3377, an intermediate-luminosity elliptical. We use this sample of stars to derive the metallicity distribution function (MDF) for its halo field stars, and comment on its chemical evolution history compared with both larger and smaller E galaxies. Our ACS/WFC field spans a radial range extending from 4 to 18 kpc projected distance from the center of NGC 3377 and thus covers a significant portion of this galaxy's halo. We find that the MDF is broad, reaching a peak at $\log(Z/Z_{\odot}) \simeq -0.6$, but containing virtually no stars more metal-poor than $\log(Z/Z_{\odot}) = -1.5$. It may, in addition, have relatively few stars more metal-rich than $\log(Z/Z_{\odot}) = -0.3$,

although interpretation of the high-metallicity end of the MDF is limited by photometric completeness that affects the detection of the reddest, most metal-rich stars. NGC 3377 appears to have an enrichment history intermediate between those of normal dwarf ellipticals and the much larger giants. As yet, we find no clear evidence that the halo of NGC 3377 contains a significant population of “young” (< 3 Gy) stars.

Subject headings: galaxies: elliptical— galaxies: individual (NGC 3377)

1. Introduction

The imaging cameras on the HST have provided powerful tools to study large photometric samples of individual stars in nearby galaxies that were quite out of reach from ground-based instruments. Although even the best photometry cannot provide the level of detail that is achievable by high-resolution spectroscopy, these deep stellar samples open a valuable route to understanding the early chemical evolution of their host galaxies, compared with the much cruder information from integrated-light photometry and spectroscopy.

Among the possible target galaxies within reach of the HST, the ellipticals are of special interest because they may result from the widest possible range of formation histories, from hierarchical merging at very early times, to recent major mergers, to later growth by satellite accretion. Representative dwarf ellipticals are readily accessible within the Local Group (particularly NGC 147, 185, 205), but the Local Group gives us no examples of giant or intermediate-sized E galaxies to work with. In a series of previous papers (Harris, Harris, & Poole 1999; Harris & Harris 2000, 2002; Rejkuba et al. 2005), we presented analyses of samples of stars in the closest giant elliptical, NGC 5128. These studies cover four locations in its halo at projected distances ranging from 8 to 40 kpc. In all four of these studies the red-giant stars are clearly resolved, and in the deepest one (Rejkuba et al. 2005), even the old horizontal-branch population is reached. We found that in all four locations in the halo of this giant elliptical, the metallicity distribution of the giant stars is

¹Based on observations made with the NASA/ESA Hubble Space Telescope, obtained at the Space Telescope Science Institute, which is operated by the Association of Universities for Research in Astronomy, Inc., under NASA contract NAS 5-26555. These observations are associated with program #9811. Support for this work was provided in part by NASA through grant number HST-GO-09811.01-A from the Space Telescope Science Institute, which is operated by the Association of Universities for Research in Astronomy, Inc., under NASA contract NAS 5-26555.

clearly metal-rich (with $\langle \text{Fe}/\text{H} \rangle \simeq -0.4$) and broad, but with extremely small proportions of classically metal-poor stars (i.e. those with $[\text{Fe}/\text{H}] < -1$).

Generalizing the results for NGC 5128 to all large ellipticals may, however, be compromised by the possibility that NGC 5128 could be a major merger remnant in which the majority of its halo stars were actually formed within the metal-rich disks of its progenitor galaxies. In fact, both a major-merger or hierarchical-merging approach are capable of creating an MDF in the halo with the same basic characteristics as we observe (Bekki et al. 2003; Beasley et al. 2003). To extend the range of information we have to work with, clearly it is of great interest to obtain the metallicity distribution function (MDF), *based directly on samples of individual stars*, in other galaxies of the widest possible range of properties.

NGC 5128, at a distance of only 4 Mpc, is by far the closest easily accessible big elliptical. To reach other ellipticals, we must step to the Leo group objects at $D \sim 10$ Mpc, and then outward to Virgo ($D \sim 16$ Mpc) and Fornax ($D \sim 19$ Mpc), which have the nearest accessible large samples of target galaxies. The technological gains afforded by the step from the HST WFPC2 camera to the newer ACS, with its much higher sensitivity, spatial resolution, and field of view, now bring these more distant targets within reach (see, for example, the recent photometric work of Williams et al. (2007) to resolve the brightest ~ 1.5 mag of the red-giant branches in four globular clusters at the Virgo distance). Roughly speaking, observing the halo of NGC 5128 with WFPC2 is comparable (for the same number of HST orbits) with observing the Leo group ellipticals with ACS.

In this paper, we present new color-magnitude photometry for the halo stars in the intermediate-sized E5 elliptical NGC 3377 in the Leo group, and briefly compare its metallicity distribution function (MDF) with those of both a dwarf and a giant. NGC 3377 has a luminosity of $M_V^T \simeq -19.9$ falling between those of the Local Group dwarfs and the giant NGC 5128 that have been observed in previous studies; it therefore provides an attractive bridge in the parameter space of galaxy properties that we can add to the discussion of chemical evolution models. The key parameters for the galaxy are summarized in Table 1.

2. Observations and Data Reduction

The imaging data we use for this study were obtained in our HST program 9811. NGC 3377 is at relatively high galactic latitude and low foreground reddening ($b = 58^\circ 3$, $E_{B-V} = 0.03$) and is thus well placed for deep photometry of its halo stars, as free from field contamination and foreground absorption as we can hope to have.

We used the Advanced Camera for Surveys in its Wide Field Channel, with image scale

0′′05 per pixel, to reach the maximum photometric depth and field coverage. A single field was targeted at $\alpha = 10^h47^m49^s00$, $\delta = +13^\circ55′40″0$ (J2000). This field is 3′82 southeast of the galaxy center, equivalent to $\simeq 12$ kpc projected linear radius. Since the effective radius of the galaxy light profile is $R_e = 1′.1$, our field is well beyond the central bulge and can plausibly be considered as giving us a first look at the genuine halo. Fields further in would obviously be of interest to track any metallicity gradient that the system might have, but would also be much more difficult to measure because of considerably increased crowding.

The filters used were the ACS/WFC “wide V” ($F606W$) and “wide I” ($F814W$), the same ones as in our previous NGC 5128 studies. The $(V - I)$ color index is a very useful metallicity indicator particularly for old red-giant stars in the range $[\text{Fe}/\text{H}] \sim -1.5$ to ~ 0 , which as will be seen below, is our main range of interest. Total exposure times were 38500 sec over 15 full-orbit exposures in $F606W$, and 22260 sec over 9 full-orbit exposures in $F814W$, adding up to a total of 24 orbits on this single field. The individual exposures were dithered over steps from 0 to 20 pixels, allowing elimination of most cosmic rays, bad pixels, and other artifacts on the detector. To prepare the images for photometry, we extracted the drizzled individual images from the HST Data Archive, registered them to within 0.05 pixels, and median-combined them. This procedure gave us a single very deep exposure in each filter. In Figure 1, we show the combined I -band image, demonstrating that the halo is well resolved into stars throughout. A small inset portion of the field is shown in Figure 2. Many faint background galaxies can be seen through the halo, but the overwhelming majority of detected objects in this field are the red giant stars of NGC 3377 itself.

To carry out the photometry on the two combined frames we used the standalone version of *DAOPHOT* in its latest (*daophot 4*) version as written by one of us (PBS). The normal sequence of *find/phot/allstar* was used, with point spread functions defined from the average of 50 to 60 stars spread across the field. The pixel coordinate systems on the two images were registered, and then the detected stars on each one were matched up to find those measured in both colors. The number density of stars on the frame was reasonably high (the average separation between detected stars is $\simeq 7$ px, while the FWHM of the point spread function is 2.3 px or 0′′115); also, differences in magnitude are not useful for deciding on matchup of stars between the V and I frames since the target stars have a very large true range in color. Matchup was therefore done by coordinates alone in a careful iterative procedure: five iterations were done with successively increasing matching radius, starting with $\Delta r = 0.2$ px and increasing to 1.5 px. In practice, more than 95% of the 75000 matches between the V and I images fell well within 1 pixel of each other.

The next step was to define the cleanest possible subset of these matches. We rejected any detected objects that fell in the regions of 5 bigger-than-average background galaxies

and one bright star, simply by masking out those regions. We also rejected objects with very poor goodness-of-fit to the PSF ($\chi_V > 2.5, \chi_I > 2.0$); and any with much larger than normal *ALLSTAR* magnitude uncertainties ($e_V, e_I > 0.25$).

Although there is a very noticeable gradient in the density of stars from the lower right portion of the field to the upper left (see Fig.1), none of the areas are excessively crowded to the point where photometry via normal PSF fitting is unusually difficult. Our data do not enter the high-crowding regime that can be found in other examples in the literature, such as (among others) the inner halo of NGC 5128 (Harris & Harris 2002), the bulge of the Local Group dwarf M32 (Grillmair et al. 1996), or the halo of the Virgo dE VCC1104 (Harris et al. 1998). Nevertheless, to extract a conservatively “uncrowded” sample of stars to work with, we calculated the nearest-neighbor distance (NND) for every measured star on both frames. We define the NND for a star simply as the distance to the closest neighboring star on the list *regardless of relative brightness*. The distribution of the NND values is shown in Figure 3, showing that the typical separation between objects is ~ 5 px or about twice the FWHM. To cull the photometry files of stars that are even mildly crowded, we decided to reject *any* object for which $NND < 3$ px, on either the *V* or *I* frames. This step removed about 17% of the *I* detections and 12% of the *V* detections. We regard the NND cutoff of 3 px as an extremely stringent choice; in fact, *allstar* has no difficulty handling cases down to $NND \sim FWHM$ or even less.

The final result of the photometry, after removal of (a) the masked regions, (b) objects with high χ and high magnitude uncertainties, and (c) stars for which any concern existed about crowding, left a total of 57039 well measured, uncrowded stars.

For calibration of the photometry, we chose to transform the filter-based magnitudes *F606W*, *F814W* into *V*, *I* in order to facilitate comparisons with previous work (Harris, Harris, & Poole 1999; Harris & Harris 2000, 2002; Rejkuba et al. 2005). First, we used the *daophot/substar* routine to subtract all but the brighter stars from the final averaged pair of images. We then obtained aperture photometry of these now-isolated bright stars to correct the *allstar* instrumental magnitudes to aperture magnitudes, and extrapolated these to large radius following the standardized prescriptions of Sirianni et al. (2005). These gave us the magnitudes *F606W* and *F814W* on the natural ACS VEGAMAG filter system. Finally, we independently derived transformations of these to the standard *VI* system by measuring an extensive set of images of the NGC 2419 standard field from the HST Archive, and comparing these with ground-based standard data in the same field. The ground-based data are part of PBS’s ongoing programme (Stetson 2000) to maintain and upgrade an all-sky system of photometric standards on the *BVRI* system of Landolt (1992). The photometry of the NGC 2419 field in particular is discussed by Stetson (2005). This remote globular cluster has

the advantages (for calibration purposes) of a blue horizontal branch at $V \sim 21$, a red giant branch tip at $(V, V-I) = (17.3, 1.50)$, and a wealth of foreground stars. The 1,257 stars adopted as standards in this field have a median of 46 groundbased observations per star in each of the V and I filters, a median standard error of 0.0054 mag in V and 0.0058 mag in I , and a magnitude and color range $12.66 < V < 22.64$, $-0.05 < (V - I) < 3.04$. Keeping quadratic terms in color index, we found for these

$$F435W = B + 0.135(B - V) - 0.44(B - V)^2 \quad (1)$$

$$F606W = V - 0.265(V - I) + 0.025(V - I)^2 \quad (2)$$

$$F814W = I + 0.028(V - I) - 0.008(V - I)^2 \quad (3)$$

These equations reproduce the NGC 2419 standard stars in all bands to within a scatter $\sigma = \pm 0.03$ mag. The equation for B is not used in this paper but is listed for information. These transformations are very close to those published in Sirianni et al. (2005), and also to those derived for our NGC 5128 outer-halo field (Rejkuba et al. 2005), which were taken during the same Cycle. The final color-magnitude diagram for the complete sample of 57039 stars is shown in Figure 4 and will be discussed below.

We estimated the internal photometric uncertainties and the detection completeness through a series of artificial-star tests with the *addstar* component of *DAOPHOT*. Stars were added to the combined V and I images in groups of 1000 over a wide range of magnitudes; these experiments were done independently on the $F606W$ and $F814W$ images. The images were remeasured in the same way as the original frames. The fraction f of stars recovered, as a function of instrumental magnitude, is shown in Figure 5. (The magnitudes here are the filter-based ones $F606W$ and $F814W$, discussed below.) The limits of our data, defined as the magnitudes at which f drops to 0.5, are $F606W(lim) = 28.95$ and $F814W(lim) = 27.70$. The trend of f with magnitude is well described in each case by a Pritchett interpolation function (Fleming et al. 1995), an analytic function with two parameters: the limiting magnitude, and a parameter α giving the steepness of the dropoff. For these images we find $\alpha = 2.5$ for V and $\alpha = 2.7$ for I . Because of the color terms in the transformations (Eqs. 2,3), these limits in the native filter-defined magnitudes do not correspond to single V or I values, but for a giant star with a typical color of $(V - I) \simeq 2$, the limits are $V(lim) \simeq 29.4$ and $I(lim) \simeq 27.7$.

In the color-magnitude diagram of Fig. 4, the 50% completeness lines are shown. An important feature of these lines is that the limiting curve for V (the upward-slanting line on the right side of the CMD) cuts off our ability to see any extremely red stars that might actually be present; these would fall at the most metal-rich end of our metallicity distribution

function. Considerably deeper exposures in V will be needed to explore the true “red limit” of the giant stars in this galaxy. Within the limits imposed by the photometry, we explicitly take into account the completeness fraction f in our derivation (below) of the metallicity distribution. As will be seen later, the completeness cutoff may affect how much of the metal-rich end of the MDF is ultimately detectable.

We find that the 50% completeness level does not change significantly with radius R from galaxy center, except perhaps marginally in the region $R < 2'$ of highest crowding. A visual confirmation is shown in Figure 6, where we subdivide the CMD data into four radial regions. The placements of the completeness cutoffs do not change relative to the distribution of stars (we will further justify this point in the later discussion on the radial gradient of the metallicity distribution). A further indication of the relative importance of crowding is shown in Figure 7, where we show the local sky intensity around each measured star (in digital units, directly as returned by *allstar*) as a function of radius from the center of NGC 3377. The inward increase becomes steeper within $R = 2'$, but the net change over the entire frame is quite modest. However, in the discussion that follows (for the distance measurement and the metallicity distribution function), to remove any residual concerns about crowding issues we further restrict our analysis to the “safest” region $R > 2'$.

The random uncertainties of the photometry, as derived from the artificial-star tests, are shown in Figure 8. The rms uncertainty rises smoothly with magnitude in a roughly exponential manner, shown by the curves in the Figure. These have equations $\sigma(V) = 0.05 \exp((F606W - 26.00)/1.8)$ and $\sigma(I) = 0.05 \exp((F814W - 25.5)/1.3)$. In the analysis, we make no use of the data fainter than the 50% completeness level (marked by the vertical line in the figures). Finally, in Figure 9 we show the mean trends for systematic bias in the photometry: a sample of the artificial-star tests is plotted, showing the median difference $\Delta m = (input - measured)$ for both filters. The median lines, plotted in 0.1-mag bins, show a consistent trend for stars to be measured 0.01 – 0.02 mag too bright, a common feature of photometry of faint stars within moderately crowded fields. Fainter than the 50% completeness level, the mean curves diverge strongly to positive Δm and the photometry becomes systematically unreliable. It is important to note, however, that for the stars brighter than the completeness limit, the mean biases in the two filters run closely parallel, and the net bias in mean *color* ($V - I$) – an important consideration since the color index is our main metallicity indicator – is negligibly small and has no effect on the derivation of the MDF. In addition, the random uncertainties have no significant effect on the inferred properties of the MDF, because we use only the brightest $\simeq 1$ mag of the RGB where the intrinsic color range of the stars is far larger than the photometric scatter. At the very top of the RGB, the intrinsic spread is $\Delta(V - I) \simeq 1.6$ mag while the photometric scatter is ± 0.1 mag or less.

3. Distance Calibration

NGC 3377 is part of the Leo I group along with several other large galaxies, most of which are spiral-type. Numerous measurements of distance to these individual Leo members are in the literature from a variety of well established distance indicators including Cepheids, planetary nebula luminosity function (PNLF), surface brightness fluctuation (SBF), and the tip of the old-red-giant branch (TRGB).

NGC 3377: For NGC 3377 itself, the SBF method (Tonry et al. 2001) gives $(m - M)_0 \equiv \mu = 30.25$, while the PNLF method (Ciardullo et al. 1989) gives $\mu = 30.07 \pm 0.18$.

NGC 3379: For the single giant elliptical in Leo I, the TRGB method has been applied through HST photometry in both the optical I band and the near-infrared. The former (Sakai et al. 1997) gives $\mu = 30.30 \pm 0.27$, and the latter (Gregg et al. 2004) gives $\mu = 30.17 \pm 0.12$. The PNLF method (Ciardullo et al. 1989) gives $\mu = 29.96 \pm 0.16$, and the SBF method (Tonry et al. 2001) $\mu = 30.12$.

Large Spirals: Cepheid-based distances have been published for some of the major spirals in the group. These include $\mu = 30.01 \pm 0.19$ for NGC 3351 (Graham et al. 1997), 30.25 ± 0.18 for NGC 3368 (Tanvir et al. 1999), and 30.10 ± 0.14 (unweighted average of 27 Cepheids; Saha et al. 1999) or 29.71 ± 0.08 (Freedman et al. 2001) for NGC 3627. PNLF distances for these galaxies include $\mu = 30.05 \pm 0.16$ for NGC 3351 and 29.99 ± 0.08 for NGC 3627 (Ciardullo et al. 2002).

Treating all these Leo members as if they are at the same true distance from us and taking an indiscriminate average of all these measurements suggests a rough consensus near $\mu \simeq 30.1 \pm 0.05$, or $D \simeq 10.4$ Mpc for the group as a whole. The galaxy-to-galaxy dispersion of these measurements, which is $\sigma_\mu = 0.17$ mag, is quite similar to the typical internal uncertainties of each one and gives no strong evidence that the distance depth of the group is an important factor.

Our new photometry penetrates well into the the old-halo red giant branch of NGC 3377, with a large sample of stars, and thus provides a new opportunity to use the TRGB distance indicator rather precisely. The key parameter is the “tip magnitude” which is, physically, the luminosity of the helium flash in the core of the red giant as it reaches the top of its first ascent along the giant branch. The bolometric luminosity of the RGB tip is, fortunately, only mildly dependent on metallicity for old stars, allowing it to be turned into an accurate standard candle.

Our analysis follows the methods used in Sakai et al. (1996, 1997) and Harris, Harris, & Poole (1999), among others: we plot up the luminosity function of the RGB stars and use the de-

tailed shape of the LF in the I band to define the onset of the RGB. For stars more metal-poor than $[\text{Fe}/\text{H}] \simeq -0.7$ (which include the majority of the ones we measure here; see next section), the I band has the strong advantage that the differential bolometric correction across the top of the RGB is almost cancelled by the dependence of $M_{bol}(tip)$ on metallicity, leaving $M_I(tip)$ with only a gradual slope with increasing color.

The luminosity function is shown in Figure 10, based on 49380 stars beyond $R > 2'$ from the galaxy center. It has been smoothed with a Gaussian kernel of $\sigma_I = 0.02$ mag. Completeness corrections are quite unimportant here, since the $f = 0.5$ completeness level is $I \simeq 27.6$, much fainter than the well resolved top of the RGB. The fact that the LF rises gradually upward at the TRGB (rather than the ideal case of an abrupt jump) is a normal consequence of an intrinsically steep LF at that point, convolved with the observational photometric scatter, and adding in the smoothing effect of the slight downward slope of the tip toward redder colors, and a small amount of field contamination, all of which act to blur out the TRGB point to some extent (see Harris et al. 1998; Harris, Harris, & Poole 1999, for detailed discussion and methodology). The actual tip is clearly somewhere near $I = 26$, but to define the true TRGB precisely, we look for a strong change in the slope of the LF as we go to fainter magnitudes across the tip. The numerically calculated first derivative of the LF, dn/dI , is shown in the second panel. A sharp upturn is present past $I = 26$ with well defined peaks that appear at $I = 26.2$ and 26.3 . These are independent of the precise value of the smoothing kernel within broad limits. To decide which of these to pick we use the “edge response filter” or ERF (the numerical second derivative of the LF), plotted in the lower panel of Fig. 10. Here, we adopt the first and most prominent peak at $I(tip) = 26.2 \pm 0.1$.

The distance modulus follows immediately once we apply a fiducial value for $M_I(tip)$. The most well established recent calibration from within the Milky Way is from a very large sample of stars in ω Cen (Bellazzini et al. 2004), giving $M_I(tip) = -4.05 \pm 0.12$. Calibrations based on theoretical RGB models (e.g. Salaris et al. 2002) yield values in the range -3.95 to -4.22 depending on both the details of the stellar physics and on observational constraints, but are entirely consistent with the ω Cen value, which we adopt here. We therefore obtain $(m - M)_I = 30.25 \pm 0.15$ for NGC 3377. This must be corrected for a foreground absorption of $A_I = 0.07 \pm 0.02$, giving a final TRGB distance measurement $\mu = 30.18 \pm 0.16$.

Averaging the TRGB distance in with the SBF and PNLf measurements listed above, and giving the three methods equal weights, we arrive at an average $(m - M)_0 = 30.17 \pm 0.10$, or $D = 10.8 \pm 0.5$ Mpc for NGC 3377 itself. These three methods – all based, necessarily, on the properties of the old stellar population – are in excellent mutual agreement, and we consider the distance to this system to be as well established as any in the local galactic neighborhood.

4. The Nature of the Brighter Stars

In Figs. 4 and 6 there are numerous stars scattered above the TRGB. There are $N_{bright} \simeq 1360$ such stars within $24 < I < 26$. Could these be a signature of a younger, intermediate-age population ($\tau \lesssim 3$ Gy), which would indicate some more recent star formation in the galaxy’s history? In Figure 11, we show the spatial distribution of these stars across our ACS field, compared with the distribution of the stars in the brightest half-magnitude of the RGB itself. Both types of stars show an obvious gradient decreasing from galaxy center, and so a significant fraction of N_{bright} must be genuine members of NGC 3377.

Before placing limits on the number of such stars that might genuinely be present, we need to rule out other possible contributors, including (a) field contamination, (b) accidental blends of two normal RGB stars, or (c) giants or AGB stars in highly evolved or temporary states including long-period variables (LPVs), which can contribute noticeable numbers of supra-TRGB stars even in an old population (see Rejkuba et al. 2003; Gregg et al. 2004, for more extensive discussion and modelling). We dealt with a similar issue for the halo stars in NGC 5128 (Harris, Harris, & Poole 1999) and found that only $\sim 1\%$ of the population there could be ascribed to the intermediate-age category.

The first option (field-contaminating objects) will include both foreground stars and faint, very small background galaxies that are near-starlike in appearance. The number of foreground stars in the direction of NGC 3377 and over the area of ACS/WFC should be $N \lesssim 20$ from Galactic models (e.g. Bahcall & Soneira 1981), but the number of faint, misidentified background galaxies is almost certainly larger and would best be measured from an adjacent ‘control’ field, which we do not have. However, we can specify a reasonable upper limit to N_{field} by using the outermost regions of our measured field. For $R_{GC} > 4'.5$ (an area of 2.78 arcmin²) there are 94 objects within $24 < I < 26$, suggesting that over the entire 11.33 arcmin² field N_{field} should be at most 376. The number density of stars is still declining at the outer edges of the field, and so this number must be a generous upper limit. Since we see 1360 such objects over the whole field, this suggests $\sim 1000 - 1200$ of them are intrinsic to NGC 3377.

Some objects could appear in this bright range because of accidental blends of two stars that are both near the upper end of the RGB. Blends like this are very likely to be responsible for much of the scatter of stars appearing just above the nominal RGB tip², but not for the

²There are $\simeq 1300$ stars in our CMD in the small interval $I = 24.0 - 24.2$ just above the RGB tip that are responsible for blurring out the definition of the TRGB and creating the smooth rolloff in the luminosity function just above the tip; see Figure 10. Most of these objects can be understood as due to blends of the brighter RGB stars with the huge number of RGB stars $\gtrsim 1.5$ mag *fainter* than the tip.

ones ~ 0.7 mag or more above it. Statistically the number of blended pairs will increase as the square of the number of stars per unit area,

$$N_{blend} \simeq \frac{N_{\star}^2 \pi q^2}{2 d^2} \quad (4)$$

where N_{\star} is the number of stars on the frame capable of generating a blended pair brighter than the TRGB, q is the radius of one resolution element, and d^2 is the area of the field. Adopting $q \simeq 2$ px, and using the fact that there are $\simeq 30000$ stars within 1 magnitude of the RGB tip, we expect $N_{blend} \sim 350$, or about one-quarter of all the objects appearing above the TRGB.

The presence of LPV-type stars is favored in an intrinsically metal-rich old population (see Rejkuba et al. 2003), and their numbers should be proportional to the total luminosity of the whole population contained in our field. Extrapolating from the stars brighter than our completeness limit with a standard Population II luminosity function, we estimate very roughly that $V(int) = 14.7$ or $L \sim 8 \times 10^7 L_{\odot}$. From Renzini (1998) we then find $N_{LPV} \simeq 400$, similar to the expected number of accidental blends. An observational confirmation that LPV-type variables should indeed be there to be found is discussed by Gregg et al. (2004), who present *HST/NICMOS* near-infrared photometry of the RGB stars in inner-halo fields for NGC 3379, the other Leo elliptical. They find (see their Table 3) that between one-quarter and one-half of the detected stars above the TRGB are variable, consistent with our rougher estimate. Rejkuba et al. (2003) found a total of more than 1100 LPVs in two fields around NGC 5128 covering an area of 10.46 arcmin², and state that these make up roughly half of the total number of stars above the TRGB, again consistent with the estimates made here.

In summary, we suggest that more than half the population of stars that lie clearly above the RGB tip are due to a combination of blends, temporary high-luminosity states of the giants, and a small amount of field contamination. The remainder not accounted for by these effects is thus $N_{bright} \sim 400 \pm 100$, or $\simeq 1\%$ of our observed total on the field. We conclude tentatively that there is no evidence for any significant “young” ($\tau < 3$ Gy) population of stars in our field.

These rough estimates are not intended to replace a more comprehensive population synthesis analysis, based on simulating the observed RGB with stars drawn from model isochrones over a complete range of ages and metallicities (see, e.g. Williams et al. 2007, for a recent example). In a later stage of this work we will develop such simulations and constrain the age range of the halo stars more completely.

5. The Metallicity Distribution

5.1. Deriving the MDF

We are now in a position to use the colors of the RGB stars to gain a first direct measurement of the metallicity distribution function (MDF) in this galaxy. To enable direct comparisons with other systems, we follow the same method as used previously for NGC 5128 and selected dwarf ellipticals (Harris, Harris, & Poole 1999; Harris & Harris 2000, 2002). A finely spaced grid of RGB evolutionary tracks is superimposed on the measured CMD, and we interpolate between these to tag every star with a heavy-element abundance Z based on its location within the tracks. As before, we use the α -enhanced tracks of Vandenberg et al. (2000), and calibrate them in terms of absolute ($V - I$) color by force-fitting them to the observed RGB sequences for Milky Way globular clusters. This approach is described in detail in Harris & Harris (2002) and we do not repeat it here. However, we emphasize that the metallicity scale we derive this way is an *observationally calibrated one* based on real globular clusters. *The theoretical RGB tracks are used only to aid interpolation between the observed sequences for real clusters*, and thus our results do not depend critically on the particular choice of stellar models. The one unavoidable and model-dependent assumption that underlies this method is that the mean age of the NGC 3377 stars is taken to be the same as for our local globular clusters (that is, about 12 Gy). If in fact they are systematically younger, then this method would slightly underestimate their Z -abundances since the RGB locus shifts blueward at lower age. However, as long as the age differences are not severe, the age correction to the MDF is small; for example, in Rejkuba et al. (2005) we note that a shift in mean age from 12 Gy to 8 Gy would produce only a 0.1-dex underestimate in $\log Z$. See also the RGB track comparisons for different ages in Harris, Harris, & Poole (1999), which demonstrate similar conclusions.

In Figure 12 we show again the composite color-magnitude diagram, but now with the RGB tracks added. The solid lines are those of the Vandenberg et al. (2000) grid, whereas the two dashed lines at right are ones for Solar ($Z = Z_{\odot}$) and $\simeq 3Z_{\odot}$ metallicities. It is clear, as we noted above, that the photometric detection limit for red stars set by the $F606W$ exposures would eliminate any giant stars at Solar metallicity or above from our sample, even if they were present. What is not obvious from this Figure is whether or not this detection cutoff imposes any more basic limit on our interpretation of the MDF; that is, are many high- Z stars actually likely to be present in this galaxy? To gain a better reply to this question, we need to look at the details of the MDF itself as far as we can gauge them.

Our derived MDF is shown in Figure 13, where we divide the sample into half-magnitude bins by approximate luminosity M_{bol} . By doing this, we test for any systematic errors in the

interpolation procedure that might result from incorrect placement of the RGB model grid on the data; we also use it to reveal any broadening of the deduced MDF from photometric scatter toward the faint end of the data. Encouragingly, we see no systematic shift in the shape of the MDF: in all three bins, the peak occurs at $\log (Z/Z_{\odot}) \simeq -0.6$, with a broad tail extending to lower metallicity and a much steeper ramp-down to higher metallicity. As we found for the giant elliptical NGC 5128 (Harris & Harris 2002), remarkably few stars are more metal-poor than $\log (Z/Z_{\odot}) = -1.5$. As a visual confirmation of this point, note directly from the CMD how few stars there are near the bluest RGB tracks, particularly at the high-luminosity end where the track color is most sensitive to metallicity. In other words, NGC 3377 – *like the giant ellipticals, but unlike the smallest dwarfs and globular clusters* – contains few stars indeed that are in the same regime as the “classic metal-poor” halo of the Milky Way. This comparison (see also the discussion below) indicates that NGC 3377 did not form simply by the amalgamation of fully-formed dwarfs.

Fig. 13 explicitly shows the MDF with, and without, photometric completeness corrections, since these are important to our assessment of the MDF. Any extremely red stars falling to the right of the $f = 50\%$ line in the CMD have been rejected from the sample, since in this region the completeness correction itself becomes dangerously large and the random and systematic errors of the photometry increase rapidly. For all stars brighter than this cutoff level, the completeness-corrected samples (the open histograms in Fig. 13) have been constructed by weighting each star individually as $(1/f)$ where $f = f_I \cdot f_V$ is the combined completeness fraction at its particular location in the CMD. For comparison, the unweighted MDF (based only on counting up all stars with $f > 0.5$) is shown in the hatched regions.

Because the 50% completeness line in V runs nearly parallel to the RGB tracks in its region, it essentially has the effect of cutting off the MDF rather abruptly at $\log (Z/Z_{\odot}) = -0.3$. Redward of this point, we have no reliable knowledge of the MDF shape. But by the time we reach this photometrically-driven cutoff, the MDF is already well past its peak frequency and declining steeply. The evidence is thus strongly suggestive that we have seen the majority of the total MDF, and that only a small fraction of its stars are at Solar-type abundance or higher. By contrast, the giant NGC 5128 has an MDF extending well up past Solar abundance, even in the outer reaches of its halo (Harris & Harris 2002; Rejkuba et al. 2005).

The fact that the V completeness cutoff is so close to the MDF peak, however, leaves lingering doubts that we have indeed seen the full shape of the metallicity distribution. Could there, in fact, be significant numbers of more metal-rich stars in the galaxy that perhaps belonged to a later star-forming episode and are still waiting to be identified? Such stars would be almost as bright in I as the other RGB stars, but would have been too red to have

been detected in V . To look into this a bit further, we have used the I –band measurements alone to isolate stars that were (a) detected and measured on the I –band image; (b) *not* detected on the V –band image; and (c) comparably bright in I to the other RGB stars. If there are large numbers of these, it would be suggestive that we have missed much of the actual RGB.

The luminosity function for the stars measured *only* in I , and passing the same photometric culling described above, is shown as the dotted line in Figure 14. This LF rises to a peak at the completeness limit $I \simeq 27.7$ and then falls steeply. By contrast, the LF for the stars measured in *both* V and I (solid line in Fig. 14, replotted from Fig. 10) has a broad peak determined by the V –band completeness limit.

Very metal-rich RGB stars (those with $\log Z/Z_\odot > -0.3$) would belong to the “ I only” LF and would lie in the approximate range from $I \simeq 26.6$ (for the very top of the RGB at $(V-I) \sim 3$) down to the I completeness limit. We see that the LF for the stars in that range (dotted line in the Figure) stays well below the LF for the stars with both V, I (solid line). In the range $26.6 < I < 27.6$, 20008 objects were measured *only* in I but not V . But this total should be considered as only an *upper* limit to the actual number of metal-rich RGB stars, because close visual inspection of the “ I only” candidates shows that a high fraction of them are small clumps of bad pixels, or faint, very small background galaxies. These passed the χ and e_I selection steps, but did not match objects appearing at the same place on the V image and thus were rejected in the construction of the CMD. Taking these into account, we make a *very rough* estimate that there are fewer than ~ 10000 genuine RGB stars redder than the completeness cutoff in our CMD. By comparison, if we employ a simple chemical evolution model to predict the shape of the entire MDF and use it to extrapolate the observed MDF up past the photometric completeness cutoff (see next section), we find that 10% of the MDF should lie at $Z > 0.5Z_\odot$, corresponding to ~ 5700 ‘missed’ stars in addition to our observed sample of 57000 over all radii. These very metal-rich stars would not change the MDF in a major way if (for example) they formed only the high-metallicity tail of the MDF that we already see. Unfortunately, any more definitive statement will have to await deeper photometry than is currently available. A clear answer would require doubling the V exposure time; that is, adding another 15 orbits to what we already have in hand. The incremental cost of HST time would thus be significant.

5.2. A Chemical Evolution Model

To step beyond the raw MDF into a simple physical interpretation, we use the basic chemical evolution model outlined in Harris & Harris (2002) (hereafter HH02) that we ap-

plied to the NGC 5128 halo and bulge stars. Similar models have also been used for the halo of the Milky Way (Prantzos 2003), and the globular cluster systems of large galaxies (Vandalfsen & Harris 2004), among other situations. This is the so-called “accreting box” model in which we assume that a region of primordial ($Z \simeq 0$) gas turns itself into stars through a long succession of star-forming episodes, all the while that more gas is flowing into the region. The rate of gas infall is assumed to die away gradually and smoothly with time, so that in the late stages of the region’s history, its chemical evolution asymptotically approaches the classic “closed box” or “simple” model. In a general sense, this model is a first-order description of what would be expected to happen during hierarchical merging of a large set of initial, pristine gas clouds, wherein star formation within the clouds is happening simultaneously with the merging into a bigger final galaxy.

In HH02 we postulate that the gas infall rate starts at a rather high level and then dies away as an exponential decay with time. We also assume that at each star formation step, the same (small) fraction of ambient gas gets turned into stars. The abundance Z of the stars forming at any given moment is then determined by the $Z(gas)$ left behind by the previous steps, in addition to the amount and composition of the new gas entering the region just before the next star formation step occurs. The sequence of timesteps can be numerically integrated to give the final distribution $n(Z)$ of the stars (see HH02 for details). The model in its simplest form has three essential and unavoidable parameters: the effective yield y_{eff} of nucleosynthesis; the initial gas infall rate relative to the amount of gas initially present in the region; and the exponential decay time for the infall.

An extremely effective way to exhibit the match between model and data is through the linear form of the MDF, as number of stars per unit heavy-element abundance Z/Z_{\odot} . The key results are shown in Figure 15, where we include stars brighter than $M_{bol} \simeq -2.5$, i.e. ones in the upper two panels of Fig. 13. As before, we include only stars at radii $R_{GC} > 2'$. The raw (shaded) and completeness-corrected (unshaded) MDF are both shown. One particular accreting-box model solution is shown as the curved line. For $Z \gtrsim 0.5Z_{\odot}$, the observed MDF is cut off by photometric incompleteness, but as noted above, this cutoff is well past the MDF peak at $Z \simeq 0.15Z_{\odot}$, and the MDF is seen to decline strongly up till the photometric cutoff.

The model fit shown in Fig. 15 is for a triad of parameters that match the *completeness-corrected* data. The effective yield is $y_{eff} = 0.0039 \simeq 0.26Z_{\odot}$; the exponential decay time for infall is 30 timesteps; and the total amount of gas infall is equal to 4 times the initial gas present in the region. The numerical integration is carried through several hundred timesteps until almost no gas remains. In each timestep we assume following HH02 that 5% of the ambient gas is converted to stars, and that the infalling gas has $Z = 0$. As we commented in

HH02, the absolute value of the timestep δt is arbitrary in this model and must be supplied by other methods; however, through various arguments about the actual rate of hierarchical merging (see again HH02), it is plausibly near $\delta t \sim 30$ Myr give or take factors of two. If so, the main period where infall is strongly influencing the MDF shape is thus the first 1 – 3 Gyr.

Each of the three critical parameters in the model controls three distinctly different features of the final MDF. First, the rapid rise in $n(Z)$ from $Z = 0$ to $Z = 0.1$ is set by the initial infall rate: the less the infall of pristine gas, the smaller the rise, until in the limit of zero infall, the $n(Z)$ curve approaches the simple exponential decline of the closed-box model, $n \sim e^{-Z/y}$. Second, the location of the peak, where the MDF turns over and begins to decline, is driven by the infall decay time: a longer decay time produces a higher- Z peak point since there is more gas to allow the enrichment process to continue driving upward. Finally, the long exponential tail to higher Z , where infall has essentially stopped and the only process left is the conversion of the remaining gas into stars (that is, a closed-box model), is shaped by the effective yield y_{eff} .

We have restricted the present comparisons to the simplest set of parameters possible within the context of the model, and the three that are the least co-dependent. But additional model parameters are possible: for example, ones introduced in our previous analysis of NGC 5128 included an initial, very short, time period τ_1 over which the gas infall is constant or rapidly ramps up; and also the assumed abundance Z_i of the infalling gas. However, these prove to be much less critical to the solution than the three primary parameters defined above. The MDF data do not have enough resolution at extremely low Z to constrain τ_1 ; and any plausibly small abundance for the infalling gas in the range $Z_i \lesssim 0.1Z_\odot$ can be used to generate adequate matches to the data (see HH02 and Vandalfsen & Harris 2004 for more extensive discussion).

The value of the effective nucleosynthetic yield at about one-quarter Solar is a factor of two or three smaller than standard y -values that would hold in a closed-box model where all the gas remains held *in situ* and where the stellar IMF and nucleosynthesis rate are normal (e.g. Pagel & Patchett 1975). But if some fraction of the gas escapes in stellar and SN-driven winds (leaky-box) then the effect is to lower y_{eff} in proportion (Binney & Merrifield 1998). Formally, our results indicate that about half the gas present in the NGC 3377 region was ejected during the successive rounds of star formation, preventing the enrichment from proceeding upward past about one-half Solar levels. For comparison, in HH02 we found $y_{eff} \simeq 0.3Z_\odot$ for the outer halo of NGC 5128, similar to the solution for NGC 3377. For the inner region of NGC 5128, much deeper in its potential well where virtually all the gas could be held, we found $y_{eff} \simeq 0.85Z_\odot$.

For systems such as these, with broad MDFs and obviously extended star formation histories, much more complex models can be clearly brought to bear. Numerous examples of such models can be found in the literature (e.g. Naab & Ostriker 2006; Romano et al. 2005; Worthey et al. 2005; Scannapieco et al. 2005; Valle et al. 2005; Lafranchi & Matteucci 2004; Oey 2000, among many recent discussions). These have been developed all the way to full hierarchical-merging and chemodynamical-evolution codes (e.g. Kawata & Gibson 2003; Cole et al. 2000; Beasley et al. 2003; Somerville & Primack 1999). In some cases very different parametric approaches are used; for example, Worthey et al. (2005) advocate the use of a closed-box model in which y_{eff} changes with time. In such a model, quite a strong decrease in y with increasing Z is necessary to reproduce the rising part of the MDF at low Z . In our view, the use of gas infall combined with $y_{eff} \simeq const$ is much more physically plausible, and has the strong advantage of employing a process (inflow of low-metallicity gas) which is almost certainly happening anyway at early times.

It is notable, however, that the minimally simple set of parameters we use here already provides an accurate first-order fit to the MDF. The interpretation we offer for the validity of our first-order model is simply that in galaxies this large, we are looking at the combined results of so many star-forming events that much of the individual detail has been averaged out and is now no longer distinguishable.

5.3. Gradients and Fine Structure?

We can also use the MDF to search for any indication of a radial metallicity gradient. Our ACS/WFC field has stars with projected radial distances from the center of NGC 3377 from 1'3 to 5'7 (4.1 kpc to 17.7 kpc), a large enough range to be worth exploring for trends. The MDF, again in its linear form, is shown in Figure 16 for an inner zone (1'3–2'0), a middle zone (2'0 – 3'5), and an outer zone (3'5 – 5'7). In each case, we show the *same chemical evolution model* applied to all three radial bins that we deduced for the total population in Fig. 15 above, simply renormalized for the different total numbers of stars.

All three panels are similar. We see no evidence for a radial gradient in metallicity, either in the peak position of the MDF or in its detailed shape. Although we deleted the innermost region $R < 2'$ in the earlier analysis to minimize random scatter in the CMD, LF, and MDF, it has not led to any systematic bias in our understanding of the metallicity structure. This is, perhaps, not a surprising result since the effective radius of the galaxy is 1'1 and thus all the stars we sample are well outside it. In NGC 5128, we found that the MDF is virtually unchanged over a radial range from ~ 10 kpc out to 40 kpc (Harris, Harris, & Poole 1999; Harris & Harris 2000; Rejkuba et al. 2005); it is only within the bulge region at $r < 8$ kpc

(for NGC 5128, $r_{eff} = 5.5$ kpc) that significant changes began showing up and the MDF became systematically more metal-rich (HH02).

Finally, we note that in either logarithmic or linear form, the MDF is very broad but contains a tantalizing hint of fine structure. The “notches” at $(Z/Z_{\odot}) \simeq 0.2$ and at $\simeq 0.3$ are statistically significant at $\gtrsim 5\sigma$ in a nominal sense (the bin at the first gap has 1000 stars whereas the smooth model would predict 1500; and the second gap has 820 stars versus 1120 expected from the model curve). Furthermore, the same gaps appear in all three of the radial bins plotted in Fig. 16. These small gaps are suggestive, perhaps, of distinct episodes of star formation that were incompletely averaged out over the whole galaxy. The extreme low-luminosity systems ω Cen and Carina show MDFs that are more sharply divided into a small number of distinct episodes (e.g. Koch et al. 2006; Sollima et al. 2005, among many others), whereas no such gaps appear in the much larger NGC 5128 (Harris & Harris 2002; Rejkuba et al. 2005). In this respect as in many others, NGC 3377 appears to occupy an intermediate position in the whole range of old, composite stellar systems: the smaller the system, the more likely it is that its MDF will be dominated by a smaller number of star-forming events and will take on a discontinuous morphology.

5.4. Comparisons with Smaller and Larger Systems

Adding this study to some of the previously cited papers, we can now make a first, admittedly rudimentary, attempt to put together a comparison of MDFs for the full range of normal E galaxies, from dwarfs to giants. An illustrative sample is shown in Figure 17. To represent the low-luminosity end of the normal E sequence, we use the “typical” Local Group dwarf NGC 147 ($M_V^T = -15.6$), with photometric (V, I) RGB data from Han et al. (1997). We also include two spatial regions from the giant NGC 5128, at $M_V^T = -22.1$: an outer-halo field at 40 kpc projected distance (Rejkuba et al. 2005), and the 8-kiloparsec “inner halo” or outer-bulge field analyzed by HH02. In all cases, exactly the same interpolation code and RGB model grid has been used to derive the MDF, so the results are internally homogeneous.

The sequence in Fig. 17 runs from the small potential well of the dwarf, through the intermediate-mass NGC 3377, to the outer regions of a giant, and finally to the deep inner regions of the giant. The change in the MDF clearly shows up as a progressively increasing spread in heavy-element abundance. We repeat that the upper tail for NGC 3377 is cut off by photometric incompleteness for $Z > 0.6Z_{\odot}$ and it is quite possible that a thin extension to higher Z is present. By contrast, the NGC 147 and NGC 5128 color-magnitude diagrams are more deeply sampled and less affected by incompleteness. In terms of physical trends, however, it is interesting to note that the *peak* of the MDF changes only modestly, from

$\simeq 0.1Z_{\odot}$ in the dwarf up to $\simeq 0.3Z_{\odot}$ in the bulge of the giant. Instead, the most prominent effect shows up in the relative number of stars at high metallicity: in the dwarf, nothing is present above $0.4Z_{\odot}$, while the MDF for the giant extends far above Solar. This is the most dramatic effect of the depth of the potential well within which their stars were forming: in the deeper wells, almost all of the gas will be retained, permitting the enrichment to continue on through many generations and go up to high Z . A secondary feature worth noting is the steepness of the rise at low Z in the two smaller galaxies, showing the importance of infalling gas. This pattern is suggestive of an interpretation that the smaller galaxies took somewhat longer to assemble than the giants, during which time the inflow of pristine gas could continue longer and have a more important effect on the final MDF.

6. Summary

We have used deep HST/ACS images of a field in the intermediate-luminosity elliptical galaxy NGC 3377, a member of the Leo group, to derive the metallicity distribution function of its stars. More than 57000 stars were measured over a radial region extending from 1'.6 to 5'.7 from galaxy center. The (V, I) data reach deep enough to reveal almost 2 magnitudes of the red-giant branch and show the expected large spread in color that accompanies a high internal dispersion in metallicity. No significant presence of any young stellar population (stars younger than a few Gyr) can be seen in the color-magnitude diagram and the interpretation of the system is relatively simple.

Using a finely spaced grid of RGB models calibrated against the Milky Way globular clusters, we derive the heavy-element abundance distribution $n(Z)$ for the NGC 3377 stars. No apparent radial gradient in metallicity shows up; in all parts of the halo, the distribution peaks at $\log (Z/Z_{\odot}) \simeq -0.6$ and is quite broad. Very few stars are, however, more metal-poor than $\log (Z/Z_{\odot}) = -1.5$, and the data suggest that few stars are more metal-rich than -0.3 . It is possible that this galaxy did not reach Solar abundance during its enrichment history, at least in its halo. The overall shape of its MDF in all respects lies between the more metal-poor dwarf ellipticals on the one hand, and the very much more metal-rich giants on the other.

WEH and GLHH thank the Natural Sciences and Engineering Research Council of Canada for financial support. We also thank an anonymous referee for constructive comments on the first version of the paper.

REFERENCES

- Bahcall, J., & Soneira, R. 1981, *ApJS*, 47, 357
- Beasley, M.A., Harris, W.E., Harris, G.L.H., & Forbes, D.A. 2003, *MNRAS*, 340, 341
- Bekki, K., Harris, W.E., & Harris, G.L.H. 2003, *MNRAS*, 338, 587
- Bellazzini, M., Ferraro, F.R., Sollima, A., Pancino, E., & Origlia, L. 2004, *A&A*, 424, 199
- Binney, J., & Merrifield, M. 1998, *Galactic Astronomy* (Princeton: Princeton Univ. Press)
- Chiappini, C., Matteucci, F., & Gratton, R. 1997, *ApJ*, 477, 765
- Ciardullo, R., Jacoby, G.H., & Ford, H.C. 1989, *ApJ*, 344, 715
- Ciardullo, R., Feldmeier, J.J., Jacoby, G.H., Kuzio de Naray, R., Laychak, M.B., & Durrell, P.R. 2002, *ApJ*, 577, 31
- Cole, S., Lacey, C.G., Baugh, C.M., & Frenk, C.S. 2000, *MNRAS*, 319, 168
- Fleming, D.E.B., Harris, W.E., Pritchett, C.J., & Hanes, D.A. 1995, *AJ*, 109, 1044
- Freedman, W.L. et al. 2001, *ApJ*, 553, 47
- Graham, J.A. et al. 1997, *ApJ*, 477, 535
- Gregg, M.D., Ferguson, H.C., Minniti, D., Tanvir, N., & Catchpole, R. 2004, *AJ*, 127, 1441
- Grillmair, C.J. et al. 1996, *AJ*, 112, 1975
- Han, M. et al. 1997, *AJ*, 113, 1001
- Harris, G.L.H., Harris, W.E., & Poole, G.B. 1999, *AJ*, 117, 855
- Harris, G.L.H., & Harris, W.E. 2000, *AJ*, 120, 2423
- Harris, W.E. 1996, *AJ*, 112, 1487
- Harris, W.E. 2001, in *Star Clusters*, Saas-Fee Advanced Course 28 (New York: Springer), ed. L.Labhardt & B.Binggeli
- Harris, W.E., Durrell, P.R., Pierce, M.J., & Secker, J. 1998, *Nature*, 395, 45
- Harris, W.E., & Harris, G.L.H. 2002, *AJ*, 123, 3108 (HH02)
- Kawata, D., & Gibson, B.K. 2003, *MNRAS*, 340, 908

- Koch, A., Grebel, E.K., Wyse, R.F.G., Kleyna, J.T., Wilkinson, M.I., Harbeck, D.R., Gilmore, G.F., & Evans, N.W. 2006, *AJ*, 131, 895
- Lafranchi, G.A., & Matteucci, F. 2004, *MNRAS*, 351, 1338
- Landolt, A.U. 1992, *AJ*, 104, 340
- Naab, T., & Ostriker, J.P. 2006, *MNRAS*, 366, 899
- Oey, S. 2000, *ApJ*, 542, L25
- Pagel, B.E.J., & Patchett, B.E. 1975, *MNRAS*, 172, 13
- Prantzos, N. 2003, *A&A*, 404, 211
- Rejkuba, M., Minniti, D., Silva, D.R., & Bedding, T.R. 2003, *A&A*, 411, 351
- Rejkuba, M., Greggio, L., Harris, W.E., Harris, G.L.H., & Peng, E.W. 2005, *ApJ*, 631, 262
- Renzini, A. 1998, *AJ*, 115, 2459
- Romano, D., Tosi, M., & Matteucci, F. 2005, *MNRAS*, 365, 759
- Saha, A., Sandage, A., Tamman, G.A., Labhardt, L., Macchetto, F.D., & Panagia, N. 1999, *ApJ*, 522, 802
- Sakai, S., Madore, B.F., & Freedman, W.L. 1996, *ApJ*, 461, 713
- Sakai, S., Madore, B.F., Freedman, W.L., Lauer, T.R., Ajhar, E.A., & Baum, W.A. 1997, *ApJ*, 478, 49
- Salaris, M., Cassisi, S., & Weiss, A. 2002, *PASP*, 114, 375
- Scannapieco, C., Tissera, P.B., White, S.D.M., & Springel, V. 2005, *MNRAS*, 364, 552
- Sirianni, M. et al. 2006, *PASP*, 117, 1049
- Sollima, A., Pancino, E., Ferraro, F.R., Bellazzini, M., Straniero, O., & Pasquini, L. 2005, *ApJ*, 634, 332
- Somerville, R.S., & Primack, J.R. 1999, *MNRAS*, 310, 1087
- Stetson, P.B. 2000, *PASP*, 112, 925
- Stetson, P.B. 2005, *PASP*, 117, 563

- Tanvir, N.R., Ferguson, H.C., & Shanks, T. 1999, MNRAS, 310, 175
- Tonry, J.L., Dressler, A., Blakeslee, J.P., Ajhar, E.A., Fletcher, A.B., Luppino, G.A., Metzger, M.R., & Moore, C.B. 2001, ApJ, 546, 681
- Valle, G., Shore, S.N., & Galli, D. 2005, A&A, 435, 551
- VanDalsen, M.L., & Harris, W.E. 2004, AJ, 127, 368
- VandenBerg, D.A., Swenson, F.J., Rogers, F.J., Iglesias, C.A., & Alexander, D.R. 2000, ApJ, 532, 430
- Williams, B.F. et al. 2007, ApJ, 654, 835
- Worthey, G., España, A., MacArthur, L., & Courteau, S. 2005, ApJ, 631, 820

Table 1. Basic Parameters for NGC 3377

Parameter	Value
<i>Type</i>	E5
α (J2000)	$10^h 47^m 42^s.4$
δ (J2000)	$13^\circ 59' 08''$
v_r (helio)	665 km s^{-1}
A_V	0.10
$(m - M)_0$	30.17 ± 0.10
V_T^0	10.23
M_V^T	-19.9

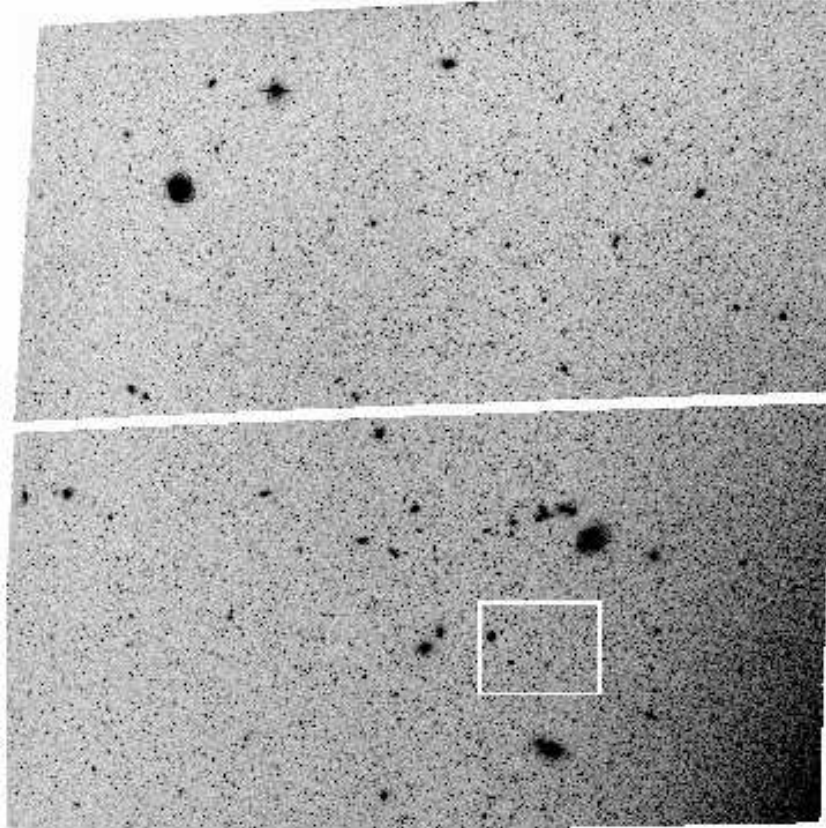


Fig. 1.— A reproduction of our measured ACS field in NGC 3377. Reproduced here is the combined $F814W$ (I band) image. At the ~ 11 -Mpc distance of NGC 3377, the ACS/WFC field size corresponds to a width of 11 kpc. The inset box shows the location of the smaller field reproduced in the next Figure. Note that the center of the galaxy is well off the field to the lower right; the ACS field center is $3'8$ away from the galaxy center.

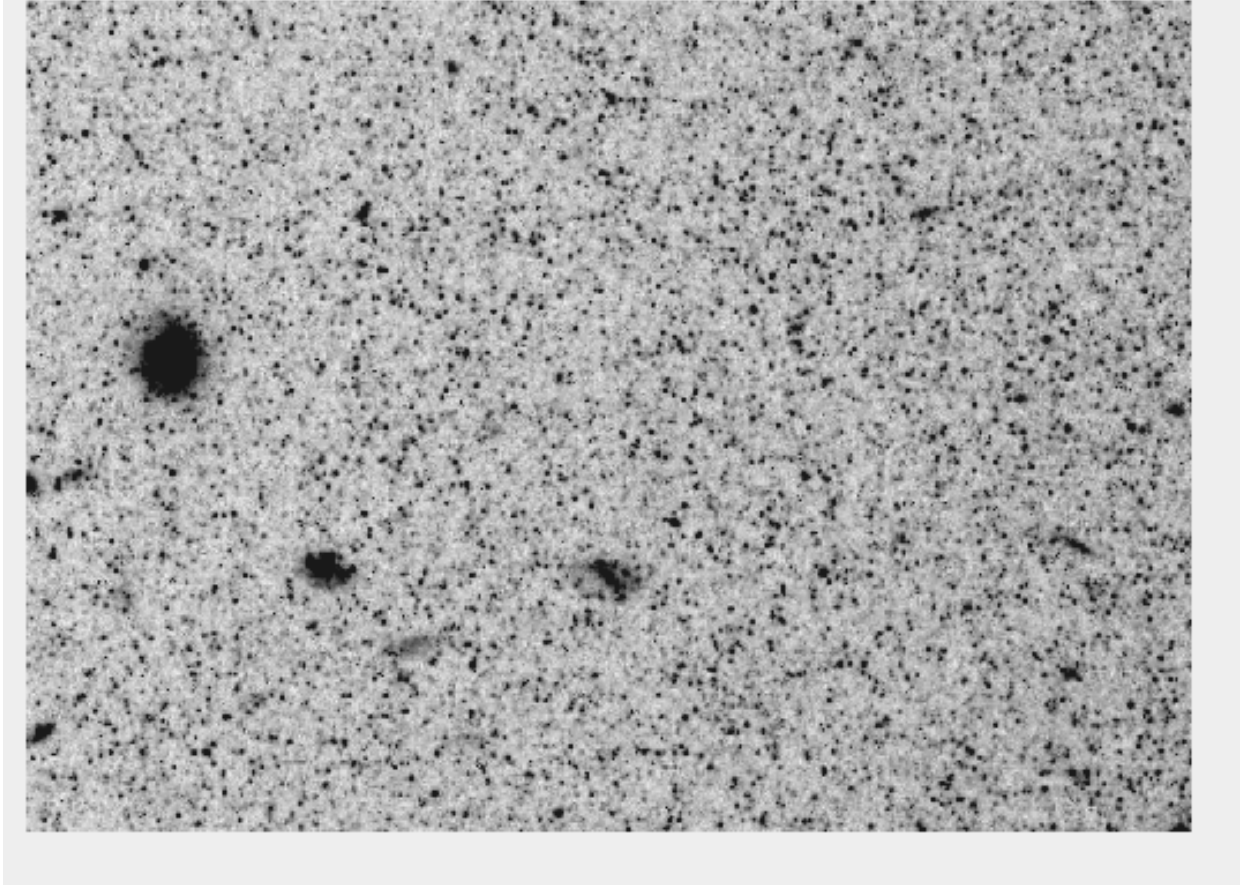


Fig. 2.— A small section of the NGC 3377 ACS field. The image shown here is from the composite I -band exposure and is $36''$ (700 pixels) wide. The halo red-giant stars are the small starlike points scattered everywhere across the field; a few distant background galaxies are also visible.

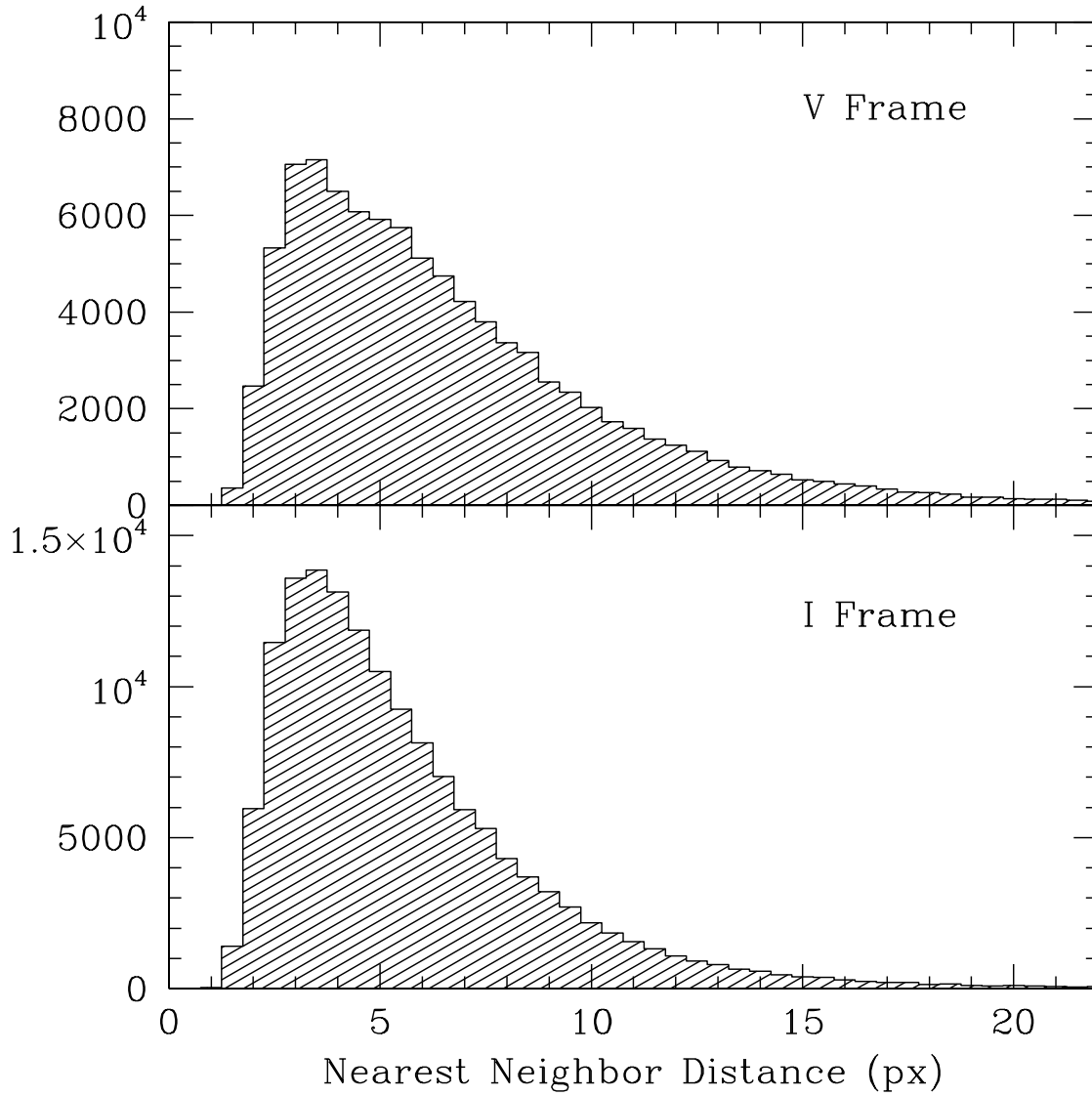
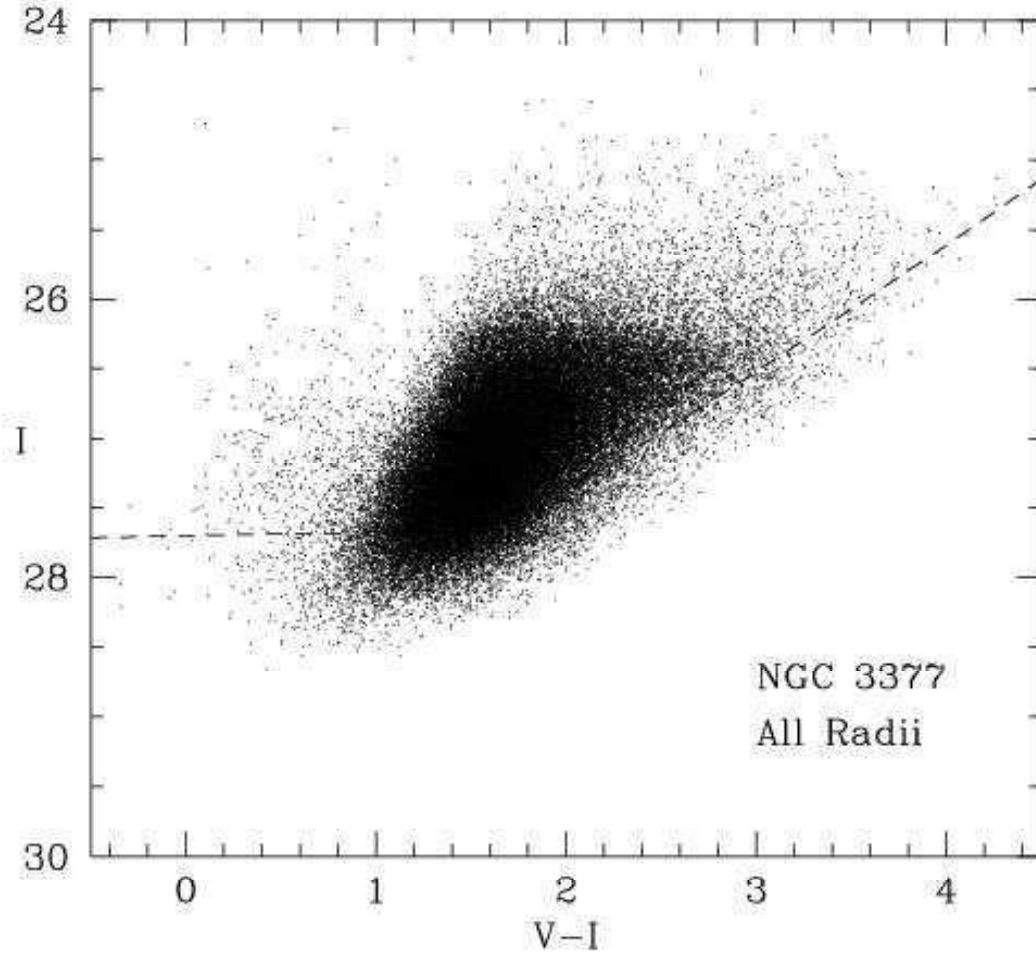


Fig. 3.— Histograms of the nearest-neighbor distances (NND) for all detected objects on each of the two frames. We reject any objects with $NND < 3$ px from the subsequent analysis to minimize any effects of crowding (see text)



f

Fig. 4.— The color-magnitude array in (V, I) for our sample of halo stars in NGC 3377. All 70,647 measured stars with high quality photometry are shown. The dashed lines show the 50% completeness limits of our measurements, as derived from artificial-star tests (see text).

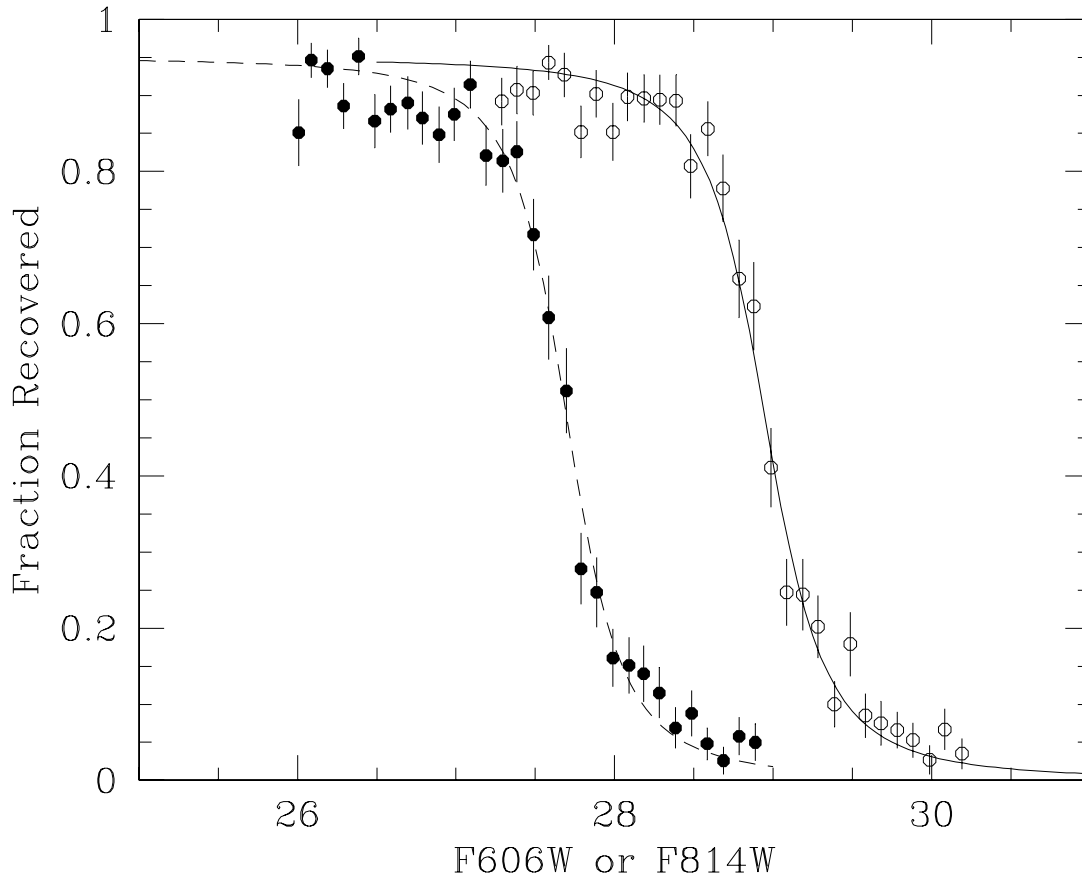
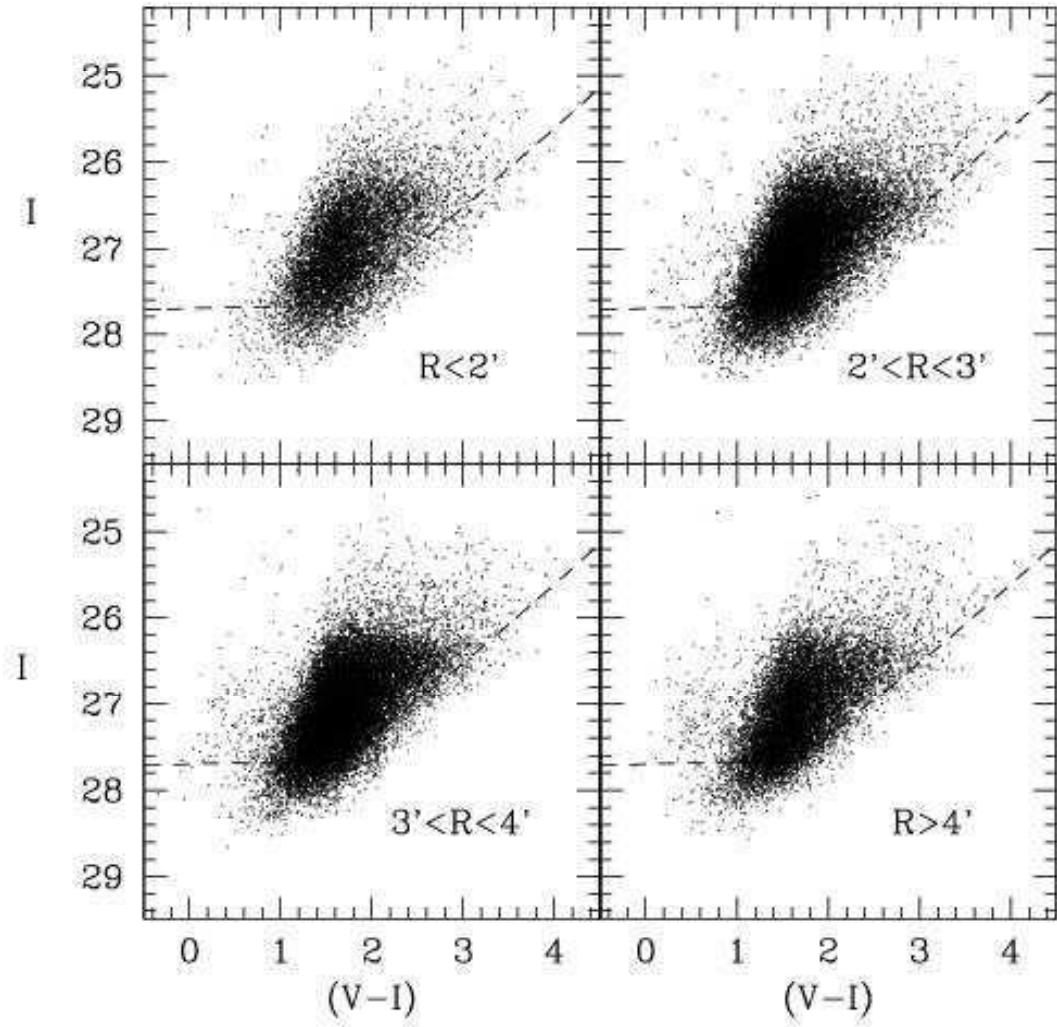
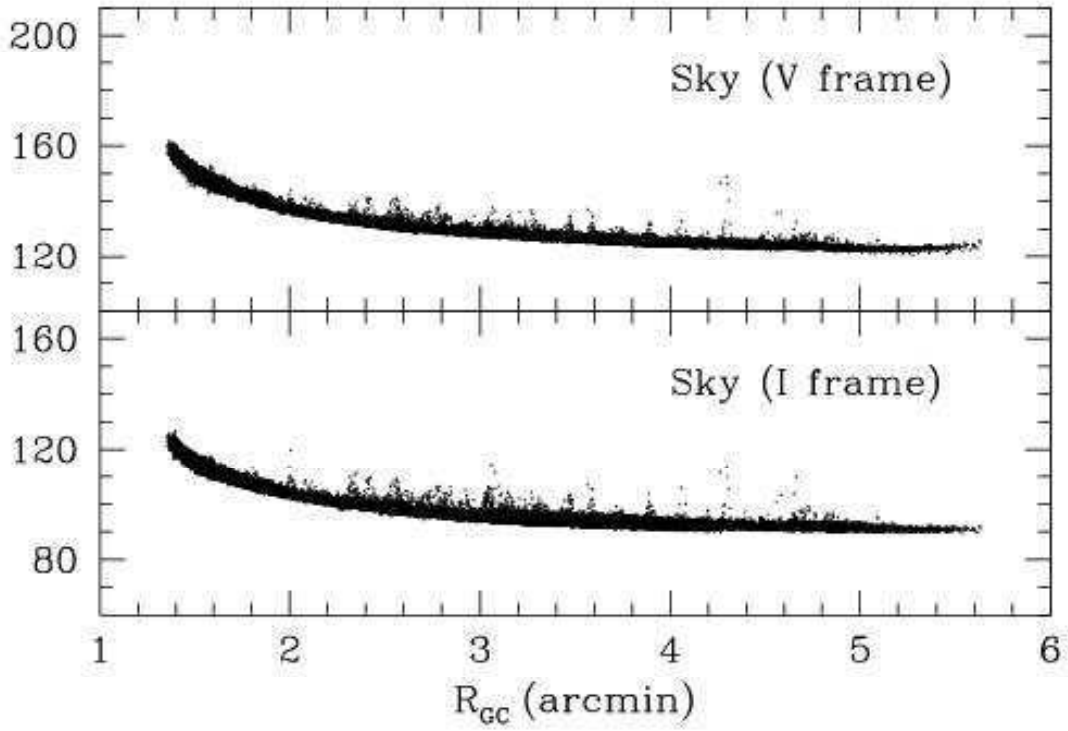


Fig. 5.— Photometric detection completeness functions, as evaluated by artificial-star experiments. The vertical axis plots the number of stars recovered by our *DAOPHOT find/allstar* measurement sequence divided by the number artificially inserted at the magnitude given along the horizontal axis. The *solid symbols* are the *F814W* (*I*-band) stars and the *open symbols* are for *F606W* (*V*-band). The fitted curves drawn through each set of points are Pritchett functions with parameters as given in the text.



f

Fig. 6.— Color-magnitude diagrams subdivided by region. Here R is the distance from the center of NGC 3377 in arcminutes.



f

Fig. 7.— Plot of the local sky intensity level as a function of radius from the center of NGC 3377. Here the vertical scale is the local sky level around each star, in units of DU as returned by *allstar*. The vertical normalization is arbitrary.

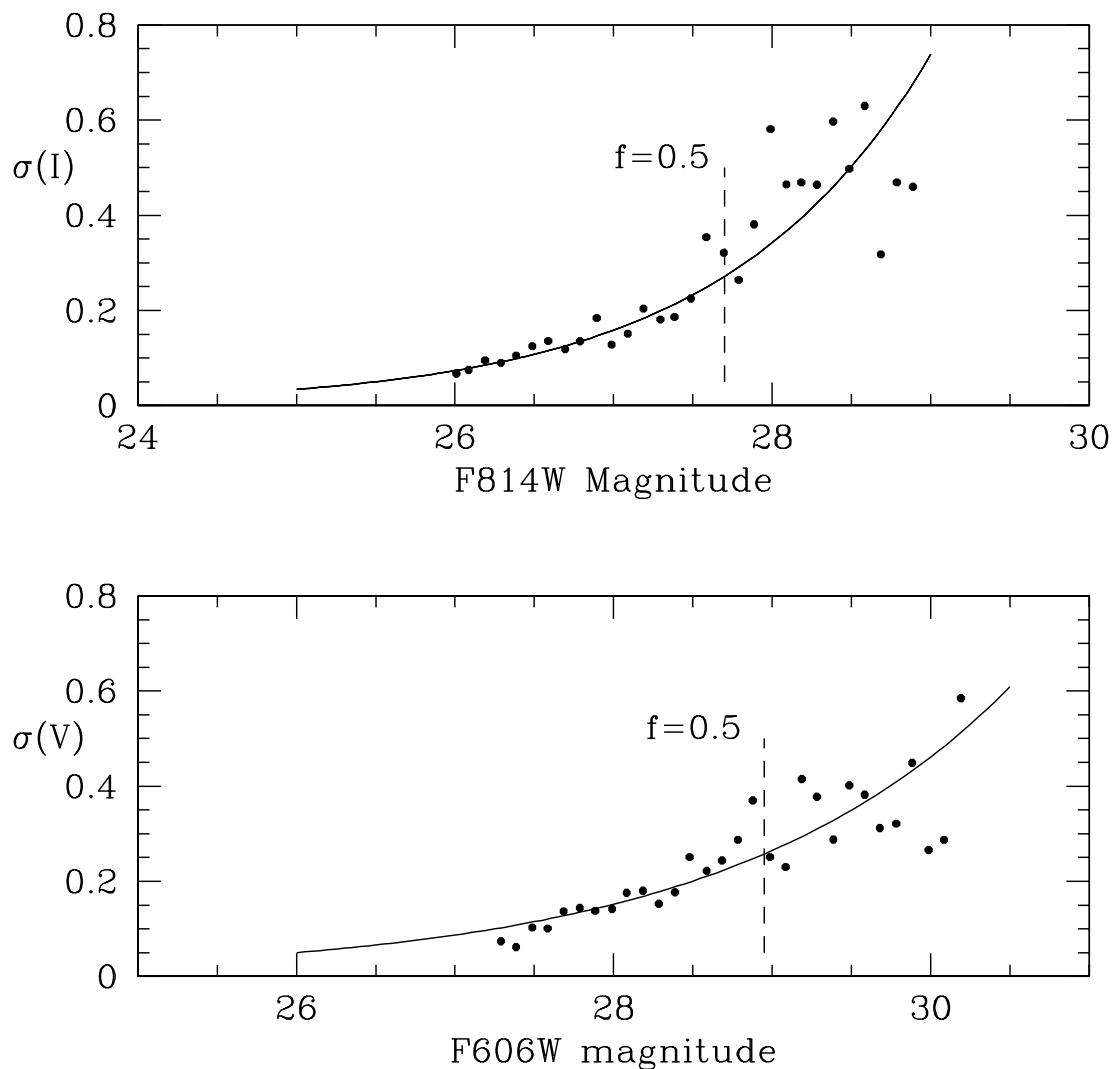


Fig. 8.— Random measurement uncertainties of the photometry, as derived from the artificial-star tests. Each plotted point (in 0.02-magnitude bins) gives the root-mean-square scatter between the input and measured magnitude for all stars in the bin. The mean lines are exponential curves with parameters as given in the text. The two vertical dashed lines show the limiting magnitudes of the photometry, i.e. the magnitude levels at which the detection completeness is 50%.

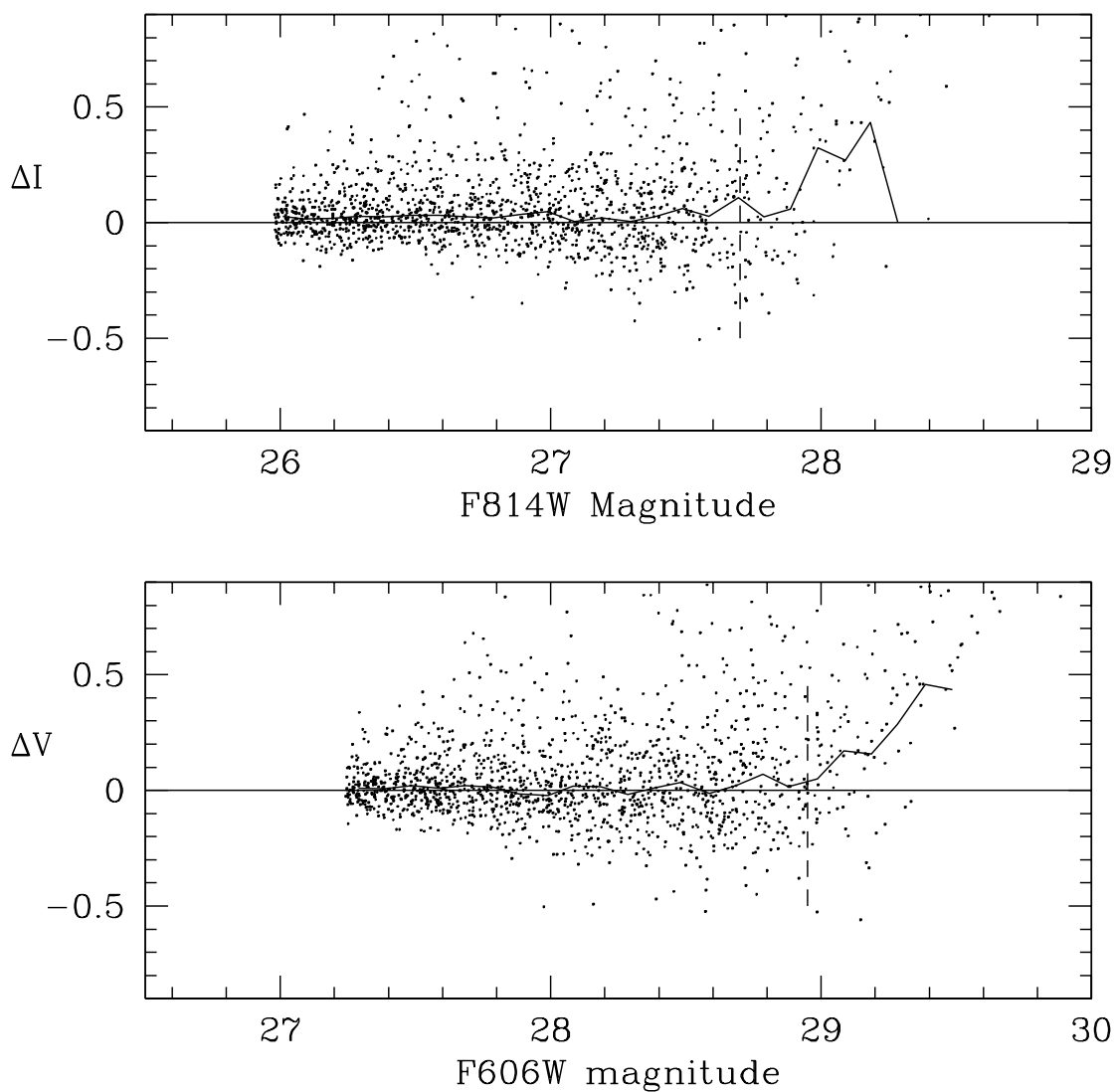


Fig. 9.— Random and systematic errors of the photometry, as derived from artificial-star tests. Each graph shows the difference between the inserted and measured magnitudes of the fake stars in the sense (input minus measured), so that stars measured “too bright” have positive values in the plot. The solid line through each plot at 0.1-magnitude bins is the median Δm within each bin. The vertical *dashed line* in each plot shows the “completeness limit” (the magnitude, from the previous figure, at which the detection completeness drops to 50 percent). Systematic errors increase dramatically for stars fainter than the completeness limit.

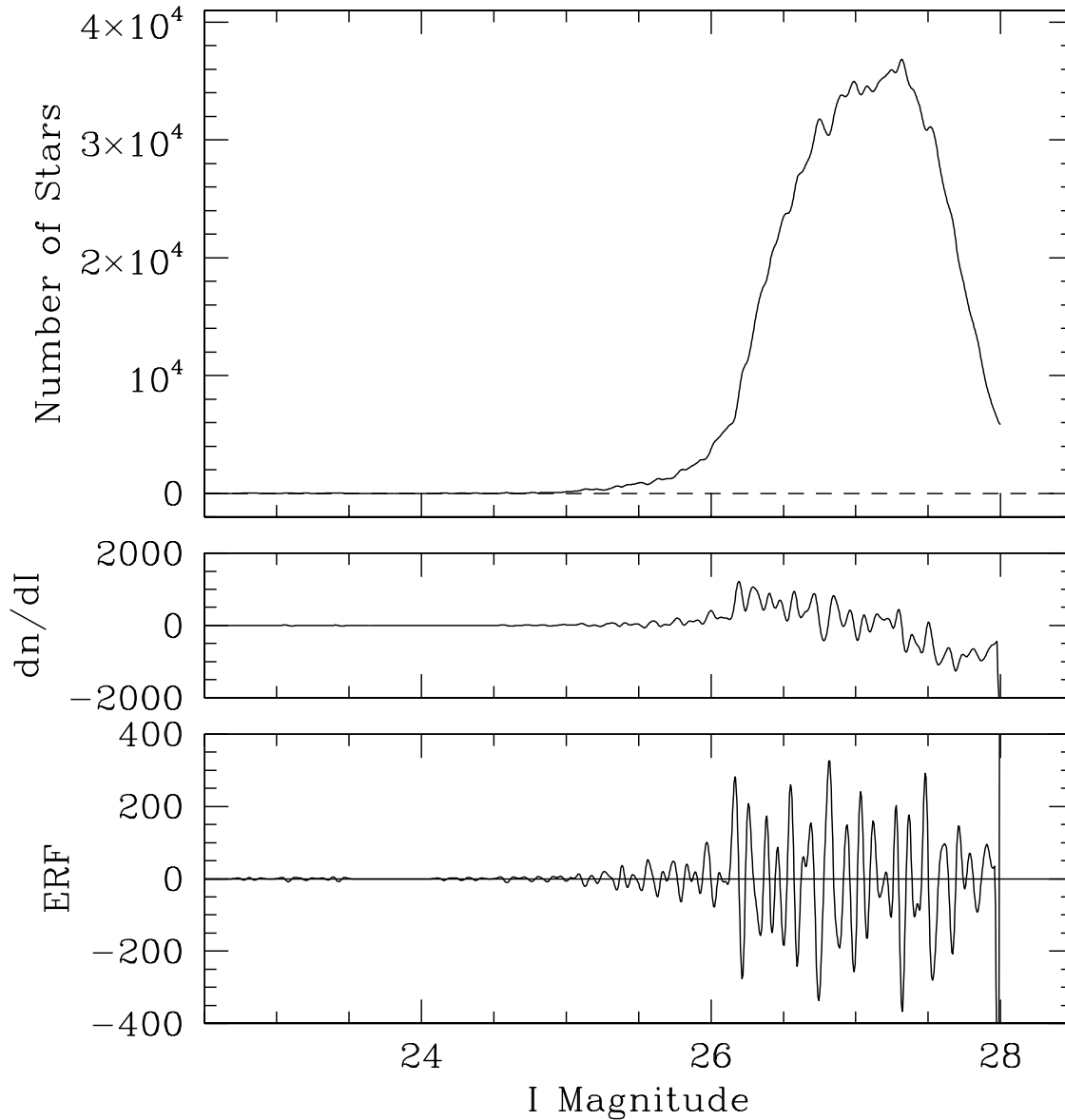
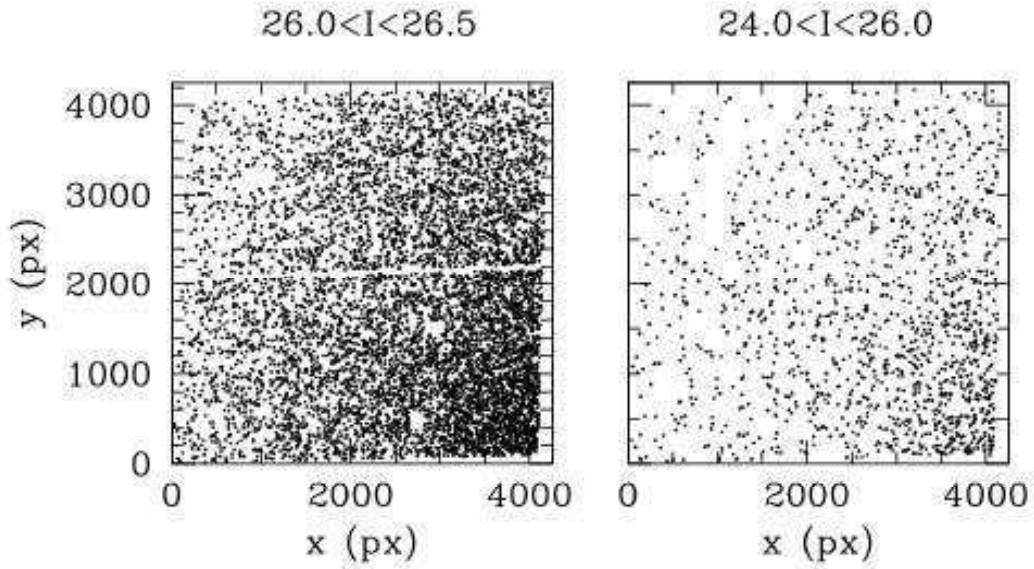
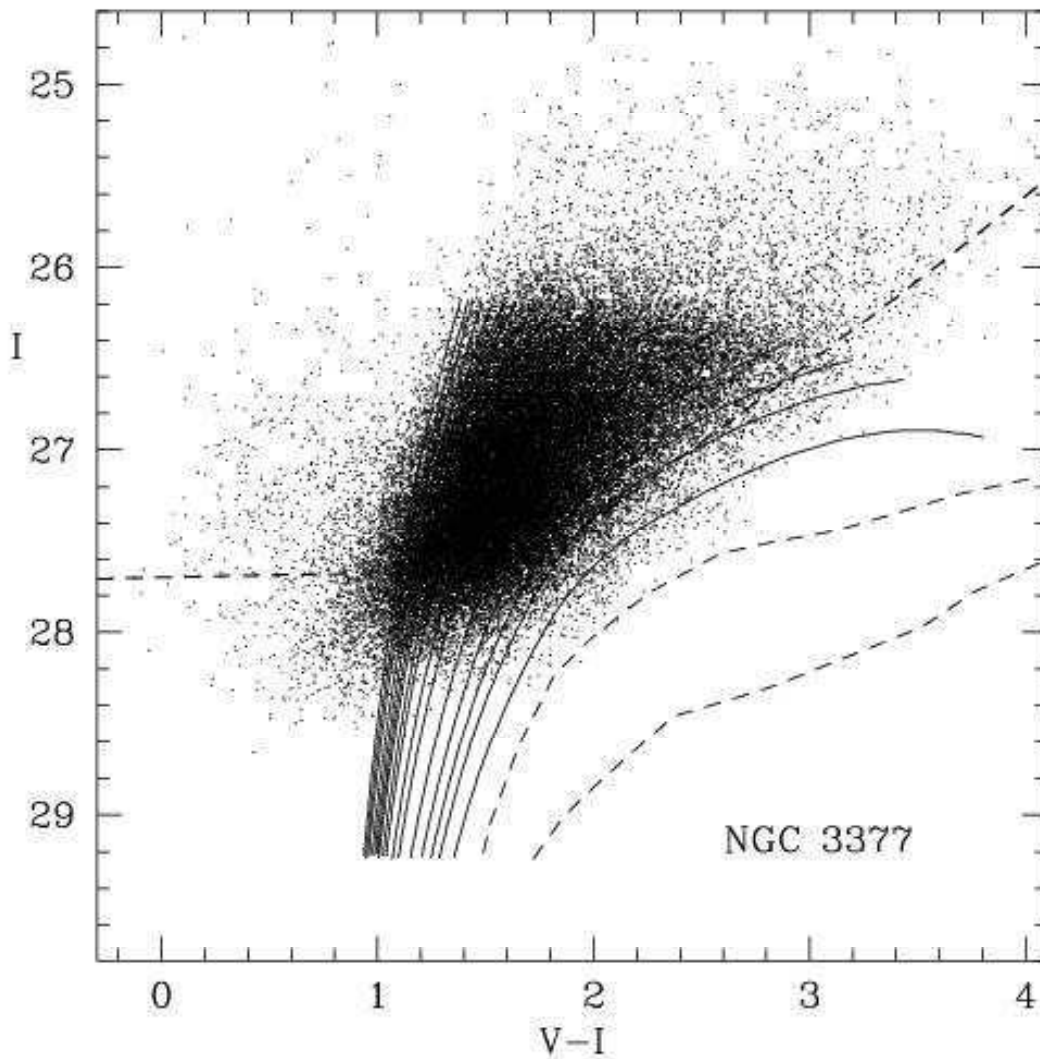


Fig. 10.— Luminosity function for all measured stars in the NGC 3377 field. In the uppermost graph, the number of stars per unit magnitude is plotted against I ; the faint-end steep decline is driven by strong photometric incompleteness. The middle panel shows our numerical estimate for the first derivative dn/dI of the LF, while the lower panel shows the numerical estimate for the second derivative d^2n/dI^2 . In all panels the data have been convolved with a Gaussian smoothing kernel of $\sigma = 0.02$ mag.



f

Fig. 11.— *Left panel:* Locations of stars in the brightest half-magnitude of the NGC 3377 red-giant branch. The location of the gap between the two ACS/WFC chips can be seen through the middle, as well as small cutout masked regions around some background galaxies. *Right panel:* Locations of stars brighter than the RGB tip.



f

Fig. 12.— Color-magnitude diagram for the NGC 3377 red giants, with model red-giant tracks superimposed on the data points. All tracks are for ages of 12 Gy, but differ in metallicity roughly in steps of $\Delta[\text{Fe}/\text{H}] \simeq 0.1$. These are the same set of tracks from Vandenberg et al. (2000) we have used for our previous study of the NGC 5128 halo, supplemented by two metal-rich tracks generated from old Milky Way star clusters (see Harris & Harris 2002), extending from $\log (Z/Z_{\odot}) = -2.0$ to $+0.4$. The placement of the tracks assumes a fore-

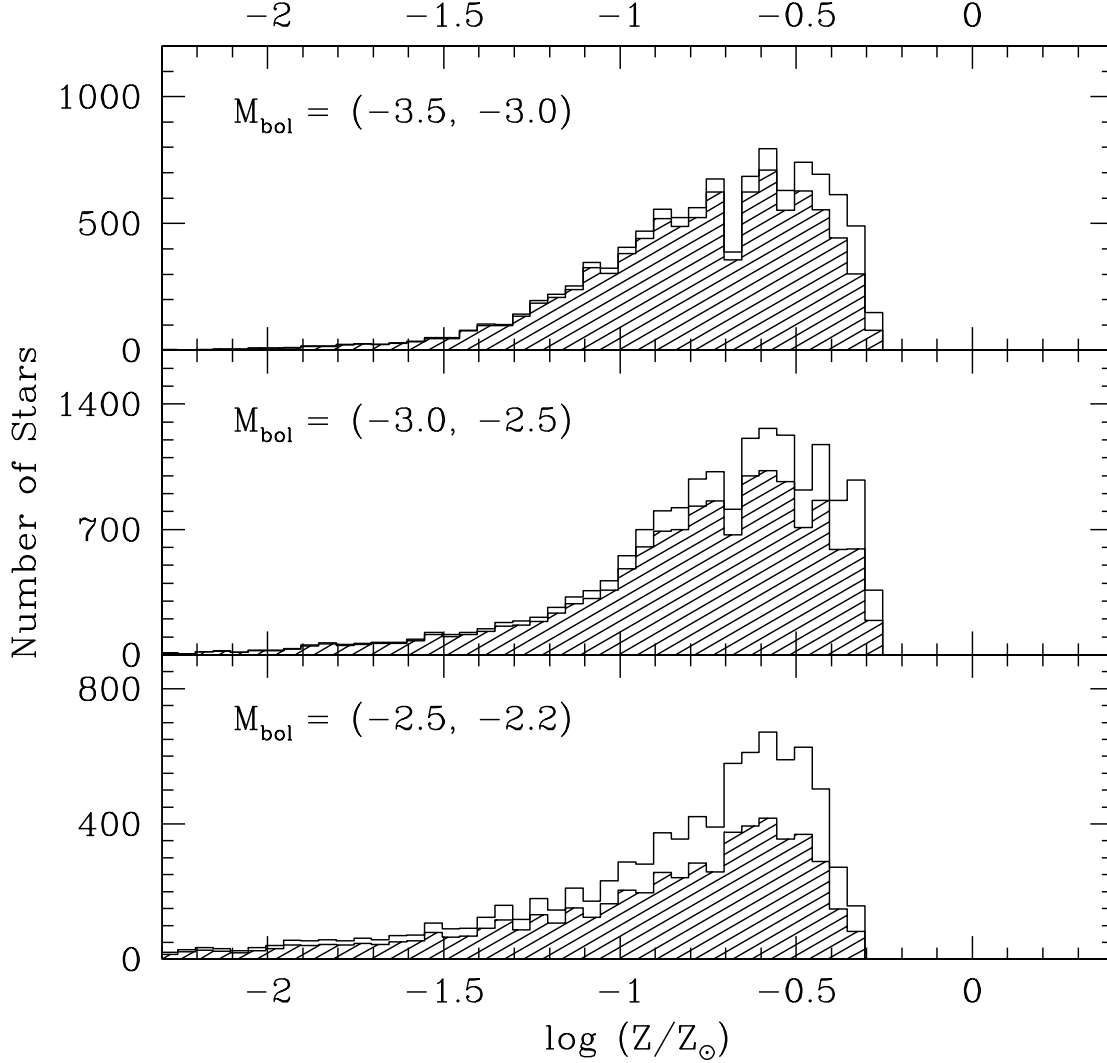


Fig. 13.— Metallicity distribution function for the halo red giants, divided into three approximate luminosity bins. This division tests for any systematic errors in the interpolation routine or the placement of the evolutionary tracks. The *shaded regions* show the MDF uncorrected for photometric completeness, while the higher *unshaded regions* show the full completeness-corrected MDF. Stars more metal-rich than $\log(Z/Z_{\odot}) \simeq -0.3$ fall to the red of the 50% photometric completeness line (see previous Figure) and are not included in the sample.

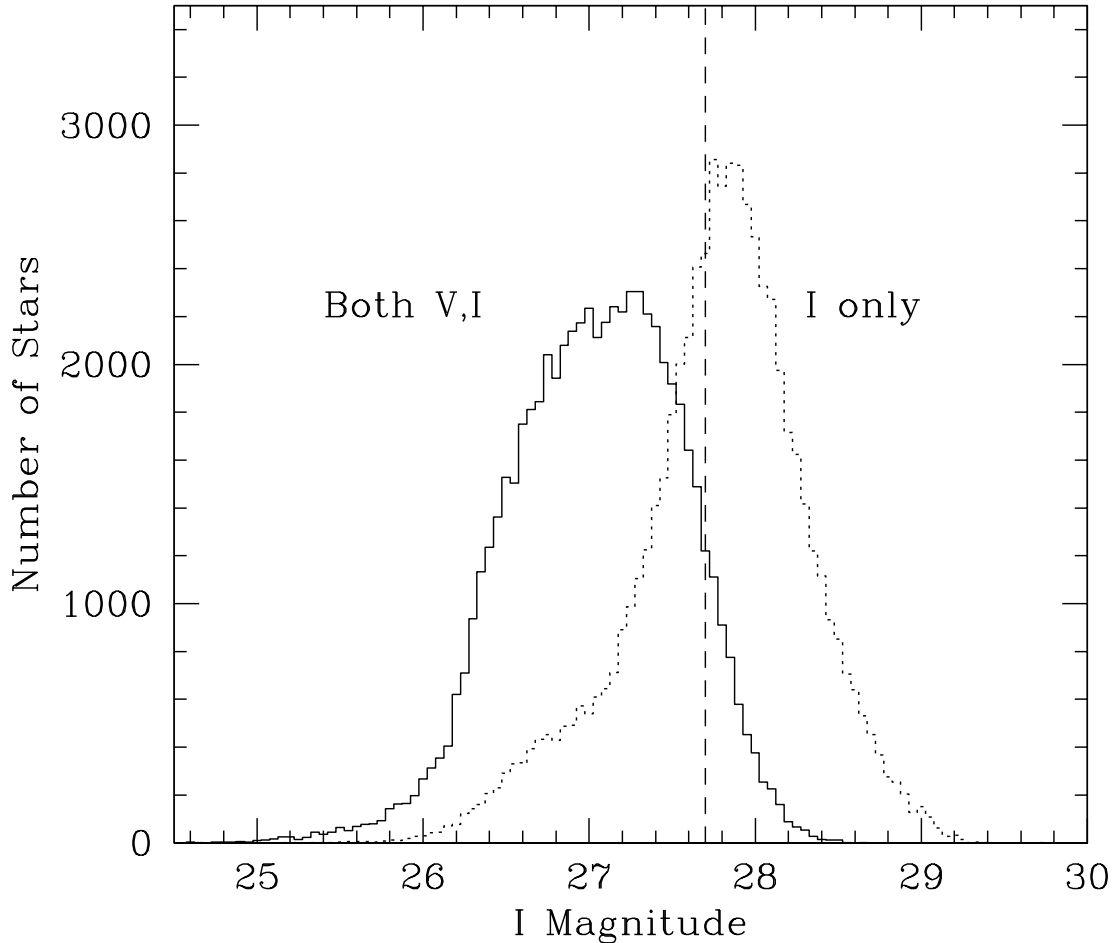


Fig. 14.— Luminosity function for the NGC 3377 stars. The vertical axis here is rescaled from Figure 10 to show the number of stars per 0.05-mag bin plotted against I magnitude. The *solid line* shows the data for the stars in the previous figure, with measurements in both V and I . The *dotted line* shows stars measured *only* in I but not in V , thus ones that do not appear in the color-magnitude diagram. The vertical dashed line at $I = 27.7$ is the 50% photometric completeness level in I . Note that for red stars measured in both V and I the detection completeness is severely incomplete fainter than $V \simeq 26.6$, thus the turnover in the solid curve is driven by the V filter cutoff.

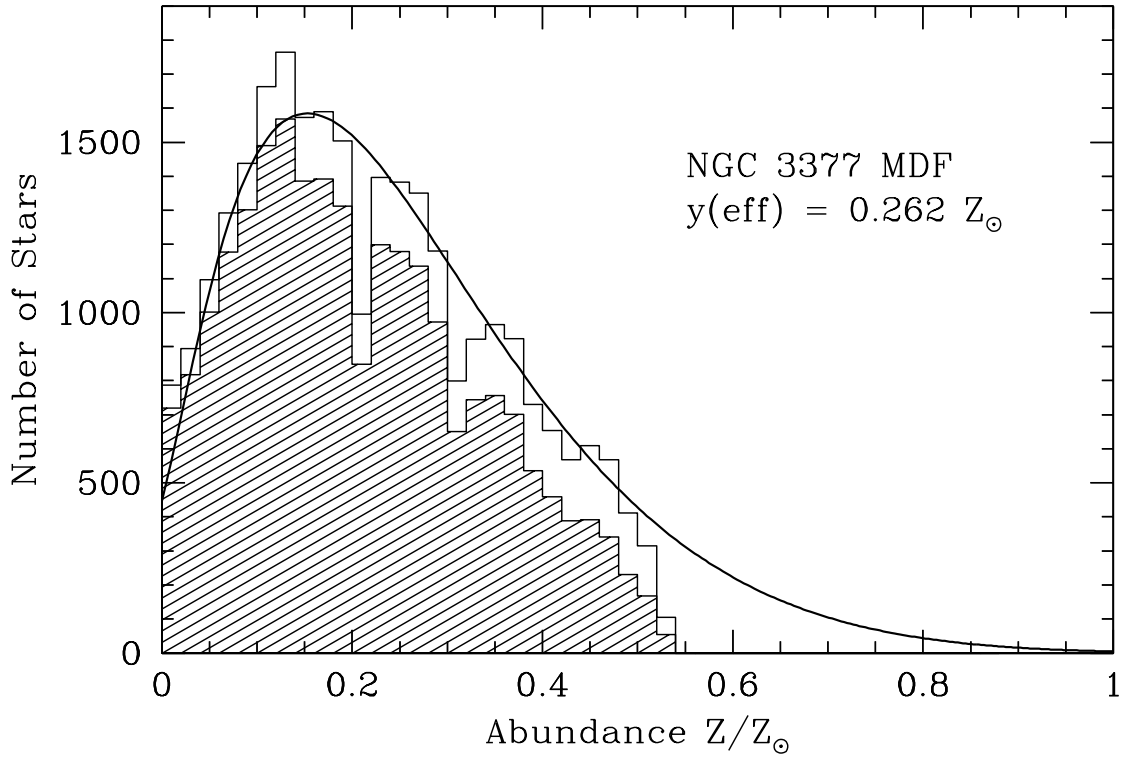


Fig. 15.— Heavy-element abundance distribution, plotted in linear form. The number of stars per unit bin $\Delta Z = 0.02$ is plotted against Z/Z_{\odot} . The solid curve is a chemical evolution model with exponentially declining infall, as discussed in the text. The assumed effective yield (the combination of stellar nucleosynthesis plus outflow; see text) is $y_{eff} = 0.0039 \simeq 0.26Z_{\odot}$.

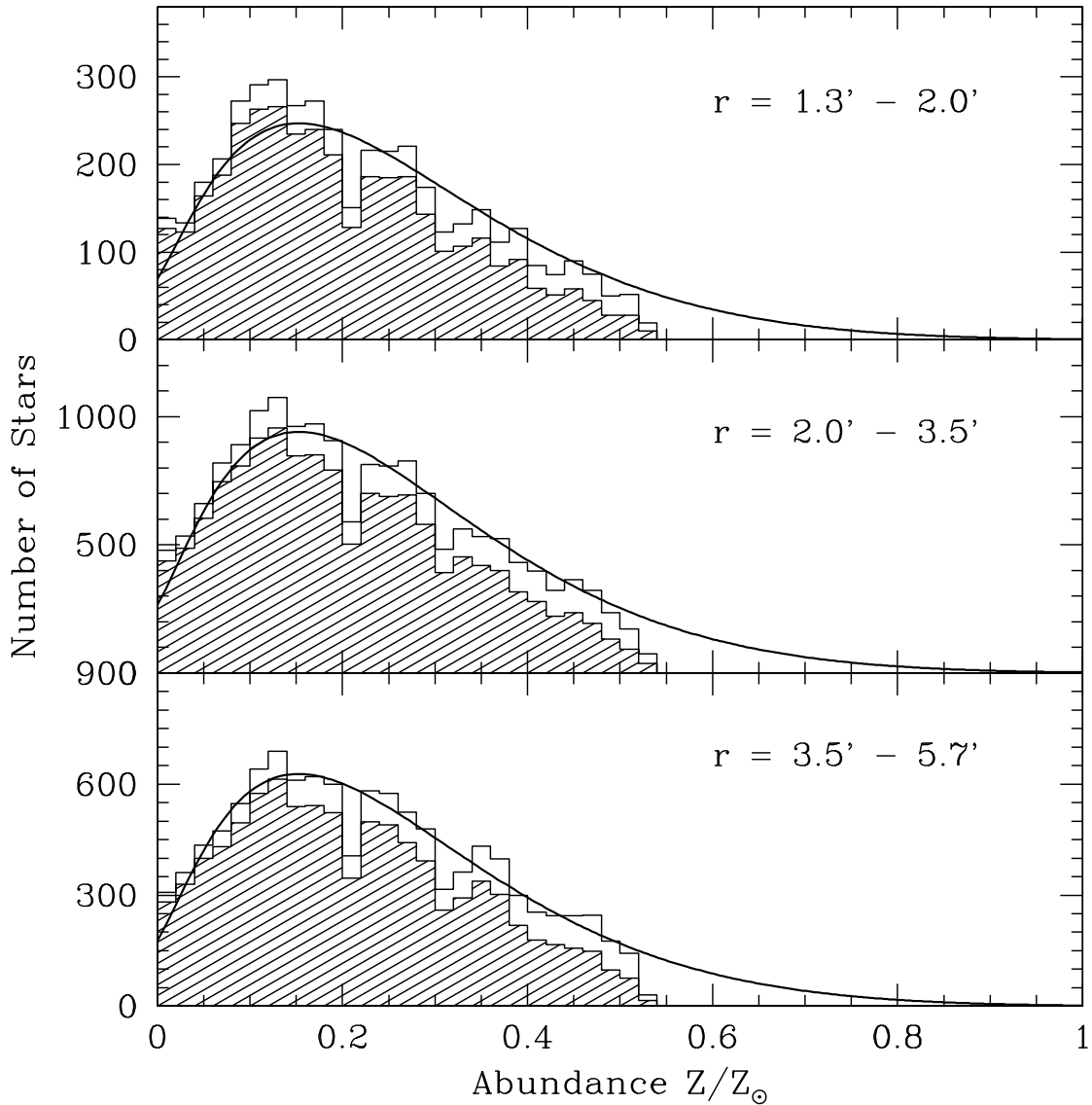


Fig. 16.— Heavy-element abundance distribution for three different radial ranges. The projected radial range in arcminutes is shown in each panel, from innermost to outermost. As in the previous Figure, the shaded region shows the raw number of stars in each Z -bin and the unshaded region the completeness-corrected bin totals. The solid curve in each case is the same chemical evolution model that was applied to the total population in the previous Figure. All three regions shown are outside the effective radius $R_e = 1.1'$ of the galaxy.

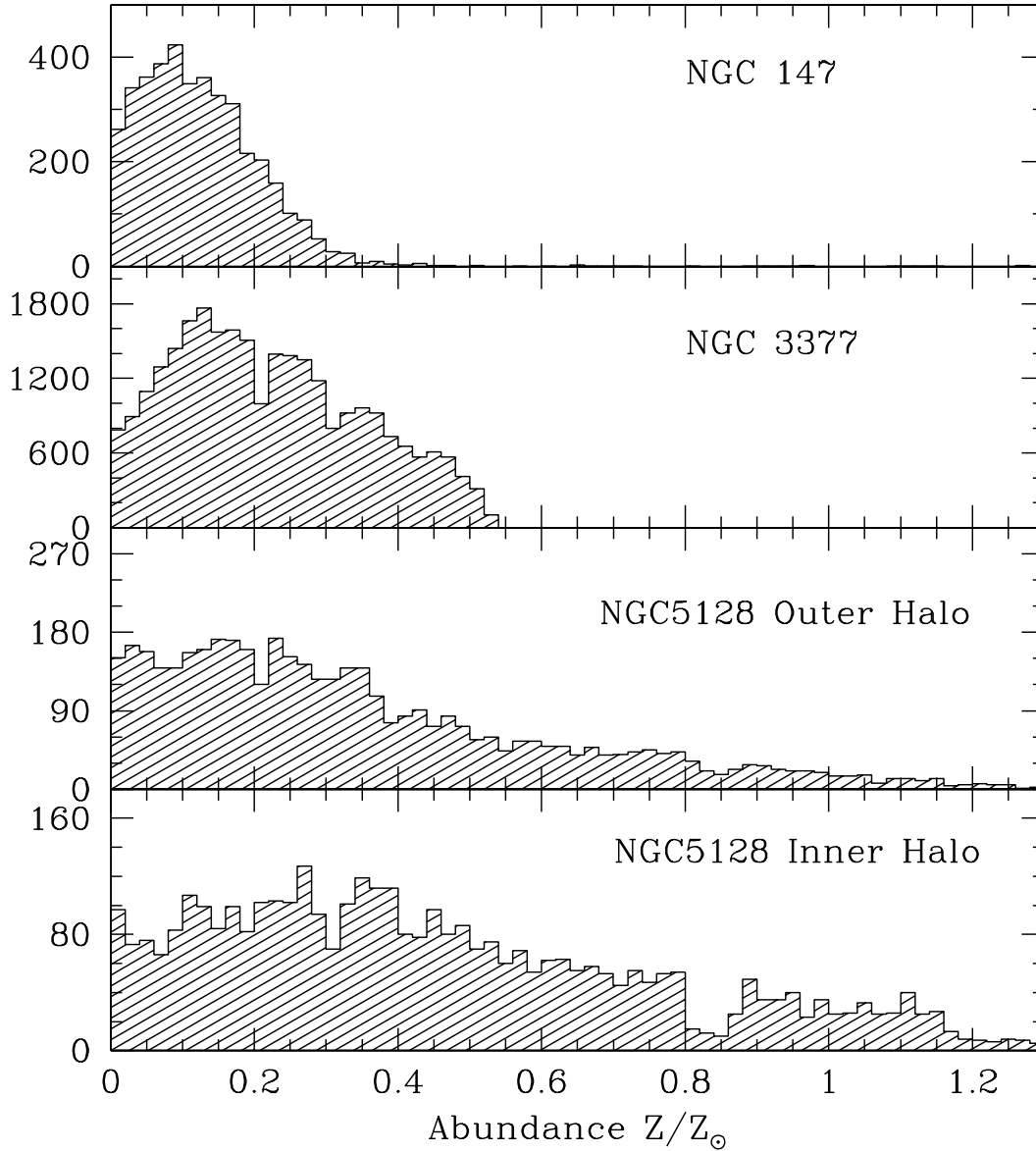


Fig. 17.— Heavy-element abundance distributions for four different samples of stars. From top to bottom these are: (a) the Local Group dwarf elliptical NGC 147, with data from Han et al. (1997); (b) the Leo elliptical NGC 3377 (this study); (c) the outer halo of the giant elliptical NGC 5128, from Rejkuba et al. (2005); and (d) the inner halo of NGC 5128, from Harris & Harris (2002).